Publication Year	2019
Acceptance in OA@INAF	2020-12-18T15:31:33Z
Title	Oxygen yields as a constraint on feedback processes in galaxies
Authors	Maritza A. Lara-Lopez; Maria Emilia De Rossi; Leonid S. Pilyugin; GALLAZZI, Anna Rita; Thomas M. Hughes; et al.
DOI	10.1093/mnras/stz2573
Handle	http://hdl.handle.net/20.500.12386/29018
Journal	MONTHLY NOTICES OF THE ROYAL ASTRONOMICAL SOCIETY
Number	490

Monthly Notices
of the
ROYAL ASTRONOMICAL SOCIETY

MNRAS **490,** 868–888 (2019)
Advance Access publication 2019 September 13

doi:10.1093/mnras/stz2573

Oxygen yields as a constraint on feedback processes in galaxies

Maritza A. Lara-López [1]★ Maria Emilia De Rossi,[2,3] Leonid S. Pilyugin,[4] Anna Gallazzi,[5] Thomas M. Hughes [6,7,8,9] and Igor A. Zinchenko [4,10]

[1]*DARK, Niels Bohr Institute, University of Copenhagen, Lyngbyvej 2, Copenhagen DK-2100, Denmark*
[2]*Universidade de Buenos Aires, Facultad de Ciencias Exactas y Naturales y Ciclo Básico Común. Buenos Aires, Argentina*
[3]*CONICET-Universidad de Buenos Aires, Instituto de Astronomía y Física del Espacio (IAFE), Buenos Aires, Argentina*
[4]*Main Astronomical Observatory, National Academy of Sciences of Ukraine, 27 Akademika Zabolotnoho St, UA-03680 Kiev, Ukraine*
[5]*INAF – Osservatorio Astrofisico di Arcetri, Largo Enrico Fermi 5, I-50125 Firenze, Italy*
[6]*Chinese Academy of Sciences South America Center for Astronomy, China-Chile Joint Center for Astronomy, Camino El Observatorio #1515, Las Condes, Santiago, Chile*
[7]*Instituto de Física y Astronomía, Universidad de Valparaíso, Avda. Gran Bretaña 1111, Valparaíso, Chile*
[8]*CAS Key Laboratory for Research in Galaxies and Cosmology, Department of Astronomy, University of Science and Technology of China, Hefei 230026, China*
[9]*School of Astronomy and Space Science, University of Science and Technology of China, Hefei 230026, China*
[10]*Astronomisches Rechen-Institut, Zentrum für Astronomie der Universität Heidelberg, Mönchhofstr. 12-14, D-69120 Heidelberg, Germany*

Accepted 2019 September 10. Received 2019 August 8; in original form 2019 May 17

ABSTRACT

We study the interplay between several properties determined from optical and a combination of optical/radio measurements, such as the effective oxygen yield ($y_{\rm eff}$), the star formation efficiency, gas metallicity, depletion time, gas fraction, and baryonic mass ($M_{\rm bar}$), among others. We use spectroscopic data from the SDSS survey, and H I information from the ALFALFA survey to build a statistically significant sample of more than 5000 galaxies. Furthermore, we complement our analysis with data from the GASS and COLD GASS surveys, and with a sample of star-forming galaxies from the Virgo cluster. Additionally, we have compared our results with predictions from the EAGLE simulations, finding a very good agreement when using the high-resolution run. We explore in detail the $M_{\rm bar}$–$y_{\rm eff}$ relation, finding a bimodal trend that can be separated when the stellar age of galaxies is considered. On one hand, $y_{\rm eff}$ increases with $M_{\rm bar}$ for young galaxies [$\log(t_{\rm r}) < 9.2$ yr], while $y_{\rm eff}$ shows an anticorrelation with $M_{\rm bar}$ for older galaxies [$\log(t_{\rm r}) > 9.4$ yr]. While a correlation between $M_{\rm bar}$ and $y_{\rm eff}$ has been observed and studied before, mainly for samples of dwarfs and irregular galaxies, their anticorrelated counterpart for massive galaxies has not been previously reported. The EAGLE simulations indicate that AGN feedback must have played an important role in their history by quenching their star formation rate, whereas low-mass galaxies would have been affected by a combination of outflows and infall of gas.

Key words: galaxies: abundances – galaxies: evolution – galaxies: fundamental parameters – galaxies: star formation.

1 INTRODUCTION

The evolution of galaxies is intimately dependent on the conversion of gas into stars, the production of heavy elements, recycling of this material into the interstellar medium, and repetitions of this cycle. A detailed understanding of the interplay between each of gas mass, star formation rate (SFR), and metallicity is clearly important to understand the galaxy evolution process.

A key variable in the gas recycling process and a primary element in the evolution of galaxies are the amount of atomic and molecular hydrogen, or H I and H_2, respectively. Large H I surveys such as the Arecibo Legacy Fast Arecibo *L*-band Feed Array (ALFALFA; Haynes et al. 2011), and the GALEX Arecibo SDSS Survey (GASS; Catinella et al. 2010), have provided H I information for thousands and hundreds of galaxies, respectively, leading to new scaling relationships and dependences in galaxies. Additionally, CO information using the IRAM 30 m telescope has been explored by the COLD GASS survey (Saintonge et al. 2011), obtaining H_2 estimates for a sample of ∼350 nearby, massive galaxies.

★ E-mail: maritza@dark-cosmology.dk

© 2019 The Author(s)
Published by Oxford University Press on behalf of the Royal Astronomical Society

Downloaded from https://academic.oup.com/mnras/article/490/1/868/5569668 by INAF Trieste (Osservatorio Astronomico di Trieste) user on 05 November 2020

Scaling relations between stellar mass and SFR (*M*–SFR), and between mass and metallicity (*M–Z*), have been explored for many years (e.g. Tremonti et al. 2004; Noeske et al. 2007; Lara-López et al. 2013a, 2009, 2010). Only during the last decade and with the advent of large surveys, multiwavelength approaches combining radio and optical observations have successfully provided critical information to investigate the connection between neutral and/or molecular gas and metallicity for large samples of galaxies. For example, Bothwell (2013) analyses the relationship between metallicity, gas content, and stellar mass of local galaxies using the data from Sloan Digital Sky Survey (SDSS) and ALFALFA, finding a fundamental relationship between those variables. Lara-López et al. (2013b) studied the relationship between cold gas, metallicity, and specific SFR through the *Z*–SSFR relationship. They found that at a given mass, and depending on the amount of gas, galaxies follow opposite behaviours; while low-mass galaxies with high/low gas fractions show high/moderate SSFR and low/high metallicities, respectively, high-mass galaxies with moderate/low gas fractions will show high/low metallicities.

Different physical explanations can be given to justify the nature of scaling relationships. Many observational and theoretical approaches have been done around the origin of the *M–Z* relation, either attributed to the presence of inflows (Dalcanton 2007), outflows (Larson 1974), differences in the star formation efficiency (SFE) of galaxies (Finlator & Davé 2008; Brooks et al. 2009; Calura et al. 2009), or variations on the initial mass function (IMF; Köppen, Weidner & Kroupa 2007).

However, the degree in which each one of them affects the metal enrichment and SFR in galaxies is still a matter of debate. For instance, Calura et al. (2009) reproduced the *M–Z* relation with chemical evolution models by increasing the efficiency of star formation in galaxies of all morphological types, without the need for outflows favouring the loss of metals in the less massive galaxies. Furthermore, Vale Asari et al. (2009) modelled the time evolution of stellar metallicity using a closed-box chemical evolution picture. They suggest that the *M–Z* relation for galaxies in the mass range from $10^{9.8}$ to $10^{11.65}$ $M_{\odot}$ is mainly driven by the star formation history and not by inflows or outflows.

On the other hand, it was pointed out in the high-resolution simulations of Brooks et al. (2009) that supernovae feedback plays a crucial role in lowering the SFE in low-mass galaxies. Without energy injection from supernovae to regulate the star formation, gas that remains in galaxies rapidly cools, forms stars, and increases its metallicity too early, producing an *M–Z* relation that is too flat compared to observations. Nevertheless, Dalcanton (2007) affirms that the fraction of baryonic mass lost through winds is quite modest (<15 per cent) at all galaxy masses. Supernova feedback is therefore unlikely to be effective for removing large amounts of gas from low-mass disc galaxies.

Another important feedback process that likely took place in the history of current massive SF galaxies is given by active galactic nuclei (AGNs). By using EAGLE simulations, De Rossi et al. (2017) showed that the slope of the *M–Z* relation is mainly modulated by stellar feedback at low masses, while AGN feedback regulates the slope at the high-mass end. In this scenario, AGN feedback would generate a decrease in the global metallicity of SF gas by quenching the star formation activity of simulated galaxies, and also by ejecting metal-enriched material.

This paper will make use of effective yields, which may indicate observationally whether a galaxy has experienced inflows and/or outflows. A galaxy that evolves as a closed box (e.g. Pagel & Patchett 1975) obeys a simple analytic relationship between the metallicity of the gas ($Z_{\rm gas}$) and the gas mass fraction $\mu = M_{\rm gas}/(M_{\rm gas} + M_{\rm star})$, where $M_{\rm gas}$ is the gas mass and $M_{\rm star}$ is the stellar mass (hereafter, $M_{\rm star}$ implies $M_{\rm star}/M_{\rm sun}$). As gas is converted into stars, the gas mass fraction decreases and the metallicity of the gas increases according to Searle & Sargent (1972) as

$$Z_{\rm gas} = y_{\rm true} \ln(1/\mu)\,, \tag{1}$$

where $y_{\rm true}$ is the true nucleosynthetic yield, defined as the mass in primary elements freshly produced by massive stars, in units of stellar mass that is locked up in long-lived stars and stellar remnants. If a galaxy evolves as a closed box, the ratio of equation (1) should be a constant equal to the nucleosynthetic yield. However, this ratio will be lower if metals have been lost from the system through outflows of gas, or if the current gas has been diluted with fresh infall of metal-poor gas. Therefore, the next ratio has been defined as effective yield:

$$y_{\rm eff} = Z_{\rm gas}/\mathrm{In}(1/\mu)\,. \tag{2}$$

The effective yield will be constant ($y_{\rm eff} = y_{\rm true}$) for any galaxy that has evolved as a closed box. The simple closed-box model assumes both instantaneous recycling and that the products of stellar nucleosynthesis are neither diluted by infalling pristine gas nor lost to the system via outflow of enriched gas (e.g. Talbot & Arnett 1971; Searle & Sargent 1972). In contrast, if any gas has either entered or left the galaxy, the effective yield will drop below the closed-box value due to changes in metallicity and/or gas mass fraction. For example, by means of an analytical chemical evolution model, e.g. Kudritzki et al. (2015) showed that high effective yield of galaxies may be explained by relatively low rates of accretion and winds. Therefore, the effective yield is an observational quantity that can be used to diagnose the addition or removal of gas in a galaxy; see Edmunds (1990) and Dalcanton (2007) for a more detailed explanation on yields.

Tremonti et al. (2004) used a sample of ∼53 000 star-forming galaxies from the SDSS at $z \sim 0.1$. By using indirect estimates of the gas mass based on the Hα luminosity, they found that $y_{\rm eff}$ decreases with decreasing baryonic mass, attributing the decrease of the effective yield at low galaxy masses to galactic winds removing metals more efficiently from the shallower potential wells of dwarf galaxies.

The direct measurement of oxygen yields requires radio observations to measure gas masses, as well as spectroscopy to measure metallicities. Then, it is natural that so far direct estimations of oxygen yields have been explored in relatively small samples. For example, by investigating the maximum metallicity value of spiral galaxies, Pilyugin, Thuan & Vílchez (2007) determined the gas metallicity through the electron temperature, obtaining an oxygen yield of about ∼0.0035. By comparing observations with analytical models, Dalcanton (2007) reached three main conclusions: (1) metal-enriched outflows are the only mechanism that can significantly reduce the effective yield, but only for gas-rich systems. (2) It is nearly impossible to reduce the effective yield of a gas-poor system, no matter how much gas is lost or accreted, and (3) any subsequent star formation drives the effective yield back to the closed-box value.

Several authors have explored effective oxygen yields for samples of dwarfs and irregular galaxies. For instance, using a sample of dwarf and irregular galaxies, Ekta & Chengalur (2010) analysed extremely metal-poor (XMP) galaxies, finding that the effective oxygen yield increases with increasing baryonic mass, consistent with what is expected if outflows of metal-enriched gas are important in determining the effective yield. Also, galaxies in their

Downloaded from https://academic.oup.com/mnras/article/490/1/868/5569668 by INAF Trieste (Osservatorio Astronomico di Trieste) user on 05 November 2020

sample deviate from the luminosity–metallicity relation due to a combination of being gas rich, and having a more uniform mixing of metals in their ISM. On the same line, Sánchez Almeida et al. (2014, 2015) have argued that the low metallicities of the extremely metal-deficient (XMD) galaxies are an indicator of infall of pristine gas. This process would increase the effective yield of low-mass galaxies as compared to more massive galaxies.

Furthermore, Garnett (2002) analysed a sample of 40 spiral and irregular galaxies with rotation speeds ranging from a few to 300 km s^{-1}. He finds that the effective yield correlates with $V_{\rm rot}$ up to $V_{\rm rot} \sim 125$ km s^{-1}. However, the $V_{\rm rot}$–$Y_{\rm eff}$ relation shows a change in slope for higher $V_{\rm rot}$ values, where there appears to be no relation. Garnett (2002) attributes this change in behaviour to increasing loss of metals from the smaller galaxies in supernova-driven winds.

Thuan et al. (2016) analysed a sample of 29 XMD blue compact dwarf (BCD) galaxies, finding that about 65 per cent of the BCDs in their sample have a $y_{\rm eff}$ larger than the $y_{\rm true}$. They explain that the most likely scenario is that the $y_{\rm eff}$ has been overestimated, since when calculating it, it is assumed that the metallicity of the neutral gas is equal to that of the ionized gas, an assumption not likely to be true. They show that the neutral gas envelope in BCDs is more metal-deficient by a factor of ∼1.5–20, as compared to the ionized gas (see also Thuan, Lecavelier des Etangs & Izotov 2005; Filho et al. 2013). The rest 35 per cent of galaxies with effective yields lower than the true yield can be understood as the result of the loss of metals due to supernova-driven outflows, and/or the consequence dilution by inflows of metal-poor gas. They find, however, that in their sample there is not an evident variation of the effective yield with the baryonic mass of the galaxy, as found by Garnett (2002), Tremonti et al. (2004), and Ekta & Chengalur (2010).

Additionally, Hughes et al. (2013) analysed the link between the gas metallicity and H I content in galaxies. They investigated the role of cold gas and environment using 260 nearby late-type galaxies from isolated to Virgo cluster members, finding a constant average effective yield of $y_{\rm eff} = 10^{-2.6}$ with a 0.2 dex scatter across the mass range. In general, they observe that gas-poor galaxies are typically more metal rich, and demonstrate that the removal of gas from the outskirts of spirals increases the observed average metallicity by ∼0.1 dex.

On the other hand, spatially resolved analyses of oxygen yields have emerged in the last years. For instance, Vílchez et al. (2019) find that the metal budget of NGC 628 and M 101 disc appears consistent with the predictions of the simple model of chemical evolution for an oxygen yield between half and one solar, although M 101 presents deviations in the outermost region, suggesting the presence of gas flow (see also Telford et al. 2019, for an analysis of M31). Also, Zasov, Saburova & Abramova (2015) analysed the radial distribution of the effective yield for a sample of 14 spiral galaxies. They show that the maximal values of the effective yield in the main discs of galaxies anticorrelate with the total mass of galaxies and with the mass of their dark haloes enclosed within R_{25}.

In this paper, we examine several scaling relations by combining several optical and radio properties, in particular for oxygen yields. This paper is organized as follows. In Section 2, we detail the data used for this study, and in Section 3 we analyse scaling relations by combining properties derived from optical and radio data. In Section 4, we analyse and compare our results with those obtained with the EAGLE simulations. In Section 5, the analysis of the relationship between $M_{\rm bar}$ and $y_{\rm eff}$ is presented. A discussion is presented in Section 6, and finally, our conclusions are given in Section 7. Throughout this paper, we assume $H_0 = 70$ km s^{-1} Mpc^{-1}, $\Omega_{\rm M} = 0.3$, and $\Omega_\Lambda = 0.7$.

2 SAMPLE SELECTION

The combination of panchromatic data represents a major step on the understanding of how galaxies assemble their mass and evolve. This paper combines optical and radio wavelengths to produce combined properties, such as gas fractions (μ), SFE, baryonic masses ($M_{\rm bar}$), and effective oxygen yields ($y_{\rm eff}$).

We consider data for emission-line galaxies from several large surveys. In optical, we use the Sloan Digital Sky Survey-Data Release 7 (SDSS-DR7; Abazajian et al. 2009) and the spectroscopic sample of the Virgo cluster from Hughes et al. (2013). In radio, we use the ALFALFA (Haynes et al. 2011) and GASS (Catinella et al. 2010) surveys to obtain H I gas, and the COLD GASS (Saintonge et al. 2011) survey to obtain H_2 information for a subsample of our galaxies. All galaxies from the GASS and COLD GASS surveys have optical counterparts from the SDSS survey. Since our sample is taken from different surveys, it presents different spatial resolutions and instrument aperture sizes. A more detailed analysis will be given using EAGLE simulations in Appendix B.

2.1 Derived properties from optical data

Data from the SDSS were taken with the 2.5 m telescope located at Apache Point Observatory (Gunn et al. 2006). We use the emission-line analysis of SDSS-DR7 galaxy spectra performed by the MPA-JHU data base.[1] From the full data set, we only consider objects classified as galaxies in the 'main galaxy sample' (Strauss et al. 2002) with apparent Petrosian r–magnitudes in the range $14.5 < m_{\rm r} < 17.77$. Additionally, we make use of the spectroscopic data from the Virgo cluster taken with the CARELEC spectrograph on the 1.93 m telescope at Observatoire de Haute Provence, as described by Hughes et al. (2013).

For reliable metallicity, SFRs, and $E(B-V)$ estimates, we selected galaxies with a signal-to-noise ratio (SNR) of 3 in Hα, Hβ, [N II], and [O III] λ5007 (Fig. 1, grey sample). Additionally, we selected only SF galaxies using the standard BPT diagram (Baldwin, Phillips & Terlevich 1981), with the discrimination of Kauffmann et al. (2003b). Our final SF optical sample for SDSS is of 252 513 galaxies (Fig. 1, blue sample). This sample is used to match with the ALFALFA, GASS, and COLD GASS data as described in Section 2.2.

For SDSS galaxies, total stellar masses were taken from the MPA-JHU data base, and are described in Kauffmann et al. (2003a). Also, SFRs and specific star formation rates (SSFRs) were taken from the same data base, and are described by Brinchmann et al. (2004). In order to identify possible biases, we compare Brinchmann et al. (2004) SFRs with two different estimations: Duarte Puertas et al. (2017), and direct integrated SFRs from the MaNGA-DR14. We find a very good agreement between them, with a mean difference between MaNGA and Brinchmann et al. (2004) of ∼0.026, and between MaNGA and Duarte Puertas et al. (2017) of ∼0.03. For further discussion, refer to Appendix A.

For Virgo cluster galaxies, we estimated SFRs based on the Hα line following the prescription of Hopkins et al. (2003) and assuming a Salpeter IMF. SFRs are corrected by Balmer decrements, stellar absorption, aperture, and obscuration as detailed by Brough et al. (2011), Gunawardhana et al. (2011), and Lara-López et al. (2013a). SFRs were converted to a Chabrier (2003) IMF by dividing them by 1.5, and converted to the Brinchmann et al. (2004) system applying

[1] http://www.mpa-garching.mpg.de/SDSS/

Downloaded from https://academic.oup.com/mnras/article/490/1/868/5569668 by INAF Trieste (Osservatorio Astronomico di Trieste) user on 05 November 2020

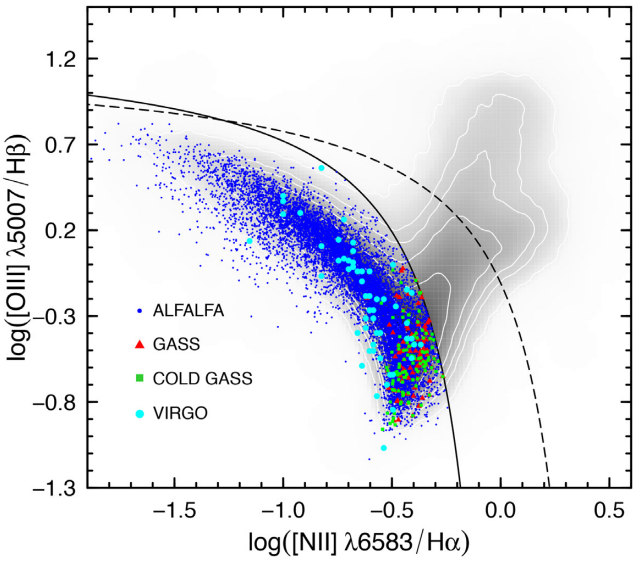

Figure 1. BPT diagram for our final sample of galaxies. Grey background data show SDSS galaxies with an S/N > 3 in the four emission lines plotted. SDSS star-forming galaxies with counterparts in the AFALFA survey are shown in blue, with the GASS survey are shown in red triangles, and the COLD GASS survey in green squares. Galaxies from the Virgo cluster are shown in cyan filled circles.

the linear conversion from Lara-López et al. (2013a):

$$\log(\mathrm{SFR})_{\mathrm{BCH}} = 0.098\,45 + 0.908\,06 \times \log(\mathrm{SFR})_{\mathrm{HOP}}\,. \quad (3)$$

SFRs for Virgo cluster galaxies are also estimated using the FUV data as described by Hughes et al. (2013). Since SFR estimations using H α and FUV agree very well, to keep consistency with the data used in this paper, we use SFRs estimated with the H α line.

To estimate gas metallicities, we use the three-dimensional calibration relations for abundance determinations from a set of strong emission lines suggested by Pilyugin & Grebel (2016). The oxygen abundances $12 + \log(\mathrm{O/H})_{\mathrm{R}}$ are determined using the R calibration (equation 4), which uses the following ratios: $\mathrm{R_2} = [\mathrm{O\,II}]\,\lambda3727 + \lambda3729/\mathrm{H}\,\beta$, $\mathrm{R_3} = [\mathrm{O\,III}]\,\lambda4959 + \lambda5007/\mathrm{H}\,\beta$, and $\mathrm{N_2} = [\mathrm{N\,II}]\,\lambda6548 + \lambda6584/\mathrm{H}\,\beta$.
The R calibration is bimodal; for $\log(\mathrm{N_2}) \geq -0.6$ (the upper branch), we have

$$12 + \log(\mathrm{O/H})_{\mathrm{R,U}} = 8.589 + 0.022\,\log(\mathrm{R_3/R_2}) + 0.399\,\log(\mathrm{N_2})$$
$$+ [-0.137 + 0.164\,\log(\mathrm{R_3/R_2}) + 0.589\,\log(\mathrm{N_2})\,] \times \log(\mathrm{R_2})$$

while for $\log(\mathrm{N_2}) < -0.6$ (lower branch) :

$$12 + \log(\mathrm{O/H})_{\mathrm{R,L}} = 7.932 + 0.944\,\log(\mathrm{R_3/R_2}) + 0.695\,\log(\mathrm{N_2})$$
$$+ [0.970 + 0.291\,\log(\mathrm{R_3/R_2}) - 0.019\,\log(\mathrm{N_2})\,] \times \log(\mathrm{R_2})\,. \quad (4)$$

It has been argued that this three-dimensional R calibration produces reliable abundances for fibre spectra from the SDSS (Pilyugin et al. 2018). It should be noted that the oxygen abundances determined through the R calibration are compatible to the metallicity scale of H II regions defined by the H II regions with abundances obtained through the direct T_{e} method. Note that for the SDSS data, we are estimating gas metallicities in a single 3 arcsec fibre spectrum per galaxy. To address the biases due to the SDSS fibre, in Appendix A we compare SDSS single fibre and integrated MaNGA IFU data for 59 common sources, finding a mean difference of ∼0.03 dex in $12 + \log(\mathrm{O/H})$.

Since the Virgo sample (and a subsample of SDSS galaxies) does not have all the emission lines to estimate directly the R calibration, we created a calibration using 7733 SDSS objects with the oxygen abundances determined through the R calibration of Pilyugin et al. (2018); we derived the following calibration for the O3N2 index:

$$12 + \log(\mathrm{O/H})_{\mathrm{R_{O3N2}}} = 8.546(\pm0.001) - 0.265(\pm0.001) \times \mathrm{O3N2}\,, \quad (5)$$

where the O3N2 index is defined as (Pettini & Pagel 2004):

$$\mathrm{O3N2} = \log\left(\frac{[\mathrm{O\,III}]\,\lambda5007/\mathrm{H}\,\beta}{[\mathrm{N\,II}]\,\lambda6583/\mathrm{H}\,\alpha}\right). \quad (6)$$

The mean difference between the metallicities estimated directly using Pilyugin & Grebel (2016) method and metallicities estimated from equation (5) is ∼0.01 dex, while the mean absolute percentage error (100 per cent/$n \times \sum_{i=1}^{n} |\,(y_i - \hat{y}_i)/y_i\,|$, where y is the actual value and $\hat{y}$ the predicted) is ∼0.62 per cent.

The oxygen abundance estimated from the emission lines reflects the gas-phase oxygen abundance. Nevertheless, some fraction of the oxygen is locked into dust grains. The dust depletion of oxygen increases with metallicity and is around 0.12 dex for H II regions of the Orion metallicity ($12 + \log(\mathrm{O/H}) \sim 8.5$, Mesa-Delgado et al. 2009; Peimbert & Peimbert 2010; Espíritu et al. 2017). We adopt the following simplest expression to describe the dust depletion of oxygen as a function of the gas-phase abundance:

$$\log(\mathrm{O/H})_{\mathrm{D}} = 0.08 \times [12 + \log(\mathrm{O/H})_{\mathrm{R}} - 7.0]\,. \quad (7)$$

Then, the total gas + dust oxygen abundance, used throughout this paper, is

$$12 + \log(\mathrm{O/H})_{\mathrm{T}} = 12 + \log(\mathrm{O/H})_{\mathrm{R}} + \log(\mathrm{O/H})_{\mathrm{D}}\,. \quad (8)$$

Finally, as an indicator of dust content, we estimated the colour excess $E(B-V)$ (e.g. Calzetti, Kinney & Storchi-Bergmann 1996). For its estimation, different radios from Hydrogen recombination lines can be used; for our sample, we are using H α and H β, and the prescription of Calzetti, Kinney & Storchi-Bergmann (1994) as follows:

$$E\,(B-V)_{\mathrm{gas}} = \frac{\log(R_{\mathrm{obs}}/R_{\mathrm{int}})}{0.4\,[\,k(\lambda_{\mathrm{H}\,\alpha}) - k(\lambda_{\mathrm{H}\,\beta})\,]}\,, \quad (9)$$

where the observed radio R_{obs} is the Balmer decrement (H α/H β), and the intrinsic ratio R_{int} is 2.86, taking a case B recombination (Osterbrock 1989). Finally, $k(\lambda)$ corresponds to the dust extinction curve; in this case, we use Calzetti et al. (2000), which is based on a set of starburst galaxies, appropriate for this analysis:

$$k(\lambda) = 2.659\,\left(-1.857 + \frac{1.040}{\lambda}\right) + 4.05,$$

for $0.63\ \mu\mathrm{m} \leq \lambda \leq 2.2\ \mu\mathrm{m}$, and

$$k(\lambda) = 2.659\,\left(-2.156 + \frac{1.509}{\lambda} - \frac{0.198}{\lambda^2} + \frac{0.011}{\lambda^3}\right) + 4.05,$$

for $0.12\ \mu\mathrm{m} \leq \lambda \leq 0.63\ \mu\mathrm{m}$. (10)

2.2 Combined properties from optical and radio data

ALFALFA (Haynes et al. 2011) is a blind survey of 21 cm H I emission over ∼2800 deg^2 of sky. We are using the catalogue public

Downloaded from https://academic.oup.com/mnras/article/490/1/868/5569668 by INAF Trieste (Osservatorio Astronomico di Trieste) user on 05 November 2020

version[2] $\alpha.70$, which provides ∼15 855 H I detections, of which ∼15 041 are associated with extragalactic objects. Since ALFALFA is a blind survey, we select only galaxies with Code = 1, which refers to robust, reliably detected sources. We also remove sources with heliocentric velocities $V_{\rm helio} < 100.0$, which are unlikely to be galaxies. From this subsample, we cross-match RA, DEC, and redshift for our optical sample, obtaining a total of 15 049 galaxies, from which 11 610 are classified as SF galaxies and meet the SN required described in Section 2.1.

In order to increase our H I coverage of massive galaxies, we match our SDSS SF sample described in Section 2.1 with the GASS public catalogue. The GASS survey observed a sample of ∼666 galaxies selected from the SDSS spectroscopic and GALEX imaging surveys. GASS galaxies are selected to have stellar masses greater than 10^{10} $M_{\rm star}$ and redshifts $0.025 < z < 0.05$. We use the public catalogue of H I detections, which includes 379 galaxies, from which a total of 102 galaxies belong to our SF sample described in Section 2.1. The rest of the GASS galaxies correspond to composite and AGN galaxies.

Galaxies from the COLD GASS survey (Saintonge et al. 2011) were included as well in our sample. We found a total of 366 matches with the SDSS data, from which 102 are star-forming galaxies, as shown in Fig. 1. Additionally, we included galaxies from Virgo with H I detections from Hughes et al. (2013), adding a total of 55 SF galaxies to our sample.

For SDSS/ALFALFA, SDSS/GASS, and Virgo galaxies, H_2 gas masses ($M_{\rm H2}$) were calculated using the prescription of Saintonge et al. (2011) as follows:

$$\log(M_{\rm H2}/M_{\rm H1}) = 0.45\,[\log(M_{\rm star}) - 10.7] - 0.387\,. \quad (11)$$

For galaxies with information from the COLD GASS survey, we used the $M_{\rm H2}$, estimated directly through CO as shown in Saintonge et al. (2011).

For the scaling relations analysed in this paper, gas masses are estimated as $M_{\rm gas} = M_{\rm H1} + M_{\rm H2}$, baryonic masses as $M_{\rm bar} = M_{\rm gas} + M_{\rm star}$, and gas fractions as

$$\mu = M_{\rm gas}/(M_{\rm gas} + M_{\rm star})\,. \quad (12)$$

Effective yields were estimated using equation (2) as $y_{\rm eff} = Z_{\rm gas}/\ln(1/\mu)$. The value of the oxygen abundance O/H is traditionally expressed in units of the number of oxygen atoms relative to hydrogen, while the value of $Z_{\rm gas}$ in equation (2) has units of mass fraction; we adopt the following relation given by Garnett (2002):

$$Z_{\rm gas} = 12 \times \frac{\rm O}{\rm H}\,, \quad (13)$$

where O/H is obtained from equation (8).

Finally, we proceed to estimate the SFE. There are many definitions for the SFE, taking the ratio of the SFR with respect to either the molecular gas, the neutral gas, or the gas mass (e.g. Leroy et al. 2008). Throughout this paper, we are using the global SFE, defined as SFE = SFR/$M_{\rm gas}$. Additionally, we are estimating the global depletion time as $t_{\rm dep} = M_{\rm gas}/{\rm SFR}$. A previous study analysing the different depletion times for $M_{\rm H2}$ and $M_{\rm H1}$ was performed by Saintonge et al. (2011).

For all the estimated variables in Sections 2.1 and 2.2, we estimated errors using the 'Propagate' package developed for the 'R' statistical programming language. This package performs propagation of uncertainty using higher order Taylor expansion and Monte Carlo simulation. We consistently used the errors provided by the Monte Carlo simulations for all our variables.

[2] http://egg.astro.cornell.edu/alfalfa/data/index.php

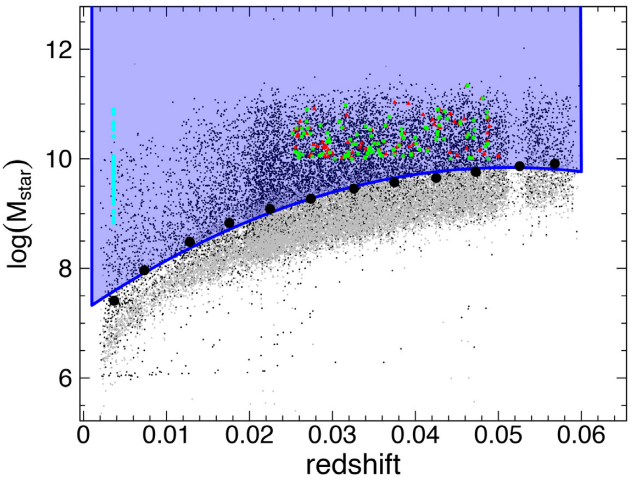

Figure 2. Stellar mass as a function of redshift for our star forming sample with ALFALFA counterparts (shown in small black dots). The stellar mass each galaxy would have if its magnitude was equal to the limit SDSS magnitude is shown in grey dots ($\mathcal{M}_{\rm lim}$). The back circles show the 95 per cent of the *M*/*L* completeness level. Galaxies from GASS, COLD GASS, and VIRGO are shown as well using the same symbols of Fig. 1.

2.3 Stellar mass completeness

Since the bulk of our sample comes from SDSS and ALFALFA counterparts, we estimated a mass completeness limit to avoid biases. The main idea is to estimate the limiting stellar mass that a galaxy could have if its magnitude corresponds to an $m_{\rm lim}$. We follow the approach by Pozzetti et al. (2010). First, we determine for all galaxies the minimum mass $\mathcal{M}_{\rm min}$, above which galaxies are complete. To derive $\mathcal{M}_{\rm min}$, we calculate the limiting stellar mass $\mathcal{M}_{{\rm lim},i}$ of each galaxy, i.e. the mass it would have, at its spectroscopic redshift, if its apparent magnitude were equal to the limiting magnitude of the survey (for SDSS $I_{\rm lim} = 17.77$, Strauss et al. 2002; Abazajian et al. 2009), given by

$$\log(\mathcal{M}_{{\rm lim},i}) = \log(M_{{\rm star},i}) + 0.4(I_i - I_{\rm lim})\,. \quad (14)$$

The result is a distribution of limiting stellar masses $\mathcal{M}_{\rm lim}$, which reflects the distribution of stellar *M*/*L* ratios at each redshift in our sample (grey dots in Fig. 2). After computing $\mathcal{M}_{\rm lim}$ for all galaxies in our sample, we selected the faintest 20 per cent in redshift bins of $\Delta z = 0.005$. Then, for each bin, we determine the mass below which lie 95 per cent of these faint objects, shown in black circles in Fig. 2. We then define $\mathcal{M}_{\rm min}$ as the upper envelope fit of the $\mathcal{M}_{\rm lim}$ distribution, as shown in the same figure. For the whole paper, we will use only galaxies above the mass completeness limit (blue shaded galaxies in Fig. 2). Galaxies below the mass completeness limit are shown in grey in Figs 4–9, 11, and 12, and are not used for any fit. In total, 6086 star-forming galaxies lie within the completeness limit.

In summary, we have 6086 star-forming galaxies with SDSS/ALFALFA counterparts within the completeness limit, 102 SDSS/GASS counterparts, 102 SDSS/COLD GASS counterparts, and 55 galaxies from the Virgo cluster. The distribution of the main properties for our final sample of SF galaxies is shown in the histograms of Fig. 3, where the blue histograms show the galaxies within the completeness limit, and the grey histograms

Downloaded from https://academic.oup.com/mnras/article/490/1/868/5569668 by INAF Trieste (Osservatorio Astronomico di Trieste) user on 05 November 2020

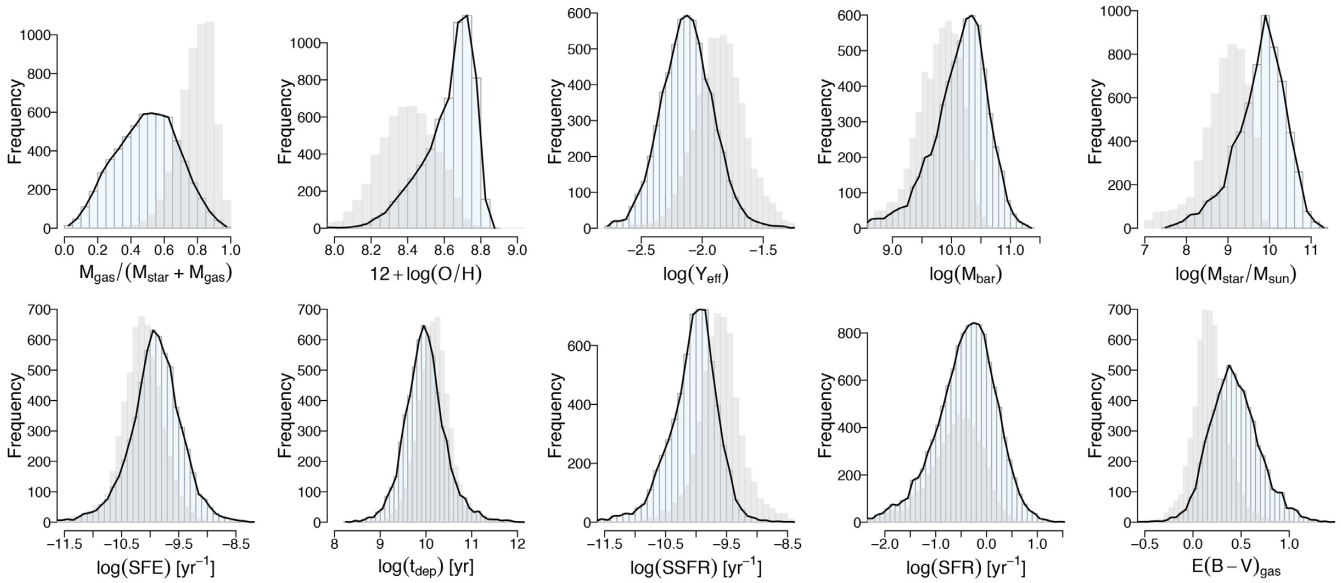

Figure 3. Histograms of all our estimated variables for our final star forming sample. The light blue histograms with solid contours show our sample within the completeness limit, while the light grey histograms show the sample outside the completeness limit.

the galaxies outside the completeness limit. From those histograms, we notice that for gas metallicities and gas fractions, the peak of the distribution is shifted considerable between galaxies within and outside the completeness limit. Since the completeness criteria are rejecting the lowest mass galaxies at a given redshift (see Fig. 2), the stellar masses of the galaxies within the completeness limit are also shifted towards higher values. This also implies that galaxies outside the completeness limit will have lower stellar masses, and hence lower metallicities, and higher gas fractions.

3 SCALING RELATIONSHIPS

In this section, we present several scaling relations from the properties derived in Section 2. First, we examine the relationship between the total oxygen abundance (estimated from equation 8) and the gas fraction (μ–Z) relation, as shown in Fig. 4. This figure has been colour coded as a function of the depletion time for all our sample. As a sanity check, we show equation (2) for an effective yield of 0.01 in solid line, 0.007 and 0.014 as dashed lines, and 0.0047 and 0.021 as dot–dashed lines. Also, we show the prediction of the closed-box model with oxygen yield $y_0 = 0.002\,68$ (or -2.57 in log units) from Pilyugin, Vílchez & Contini (2004) (red solid line). It is worth noting that ∼98 per cent of our SF sample has higher yields than the closed-box model prediction.

From Fig. 4, galaxies with low gas fraction show high gas metallicities, and are forming stars at higher efficiencies, or lower depletion times. On the other hand, galaxies with high gas fractions show low gas metallicities and longer depletion times, meaning they are inefficient at converting gas into stars. This suggests a downsizing effect in the sense that the less massive galaxies are slower in converting their mass into stars and in building up their metal content (e.g. Vale Asari et al. 2009). Furthermore, galaxies from the Virgo cluster (shown in filled larger circles) are shifted towards lower gas fractions. As discussed by Hughes et al. (2013), the most likely scenario is that the gas from these galaxies was removed, decreasing the gas fractions. Interestingly, galaxies from the Virgo cluster align very well with the closed-box model (red solid line in Fig. 4). It is important to bear in mind that the μ–Z relation and oxygen yield scales will change depending on the metallicity calibration used, although the shape of this relationship should remain very similar.

We explore as well scaling relations with the SFE as an indicator of the current efficiency in which galaxies are converting gas into stars. We find that the SFE shows a large scatter with the baryonic mass, as shown in Fig. 5 (left), although suggesting opposite trends within the scatter. Galaxies with $M_{bar} > \sim 10^{10}$ seem to show a very high dispersion, with a slight correlation with SFE, whereas galaxies with $M_{bar} < \sim 10^{10}$ show a slight anticorrelation between the same variables. Furthermore, gas metallicity seems to separate one tendency from the other, as shown in the colour gradient of the same figure, though we highlight that the dispersion is very high in the whole relation.

Scaling relations involving the SFE with stellar mass or gas fraction do not suggest any bimodality, and scale with each other with a moderate dispersion for the M_{star}–SFE relation, and a smaller dispersion for the μ–SFE relation, as shown in the centre and right-hand panels of Fig. 5, respectively. The obtained fits for the M_{star}–SFE and μ–SFE relations are:

$$\log(\mathrm{SFE}) = 0.4365(\pm 0.0154) \times \log(M_{star}) - 14.16(\pm 0.15) \quad (15)$$

with an RMSE = 0.47, and

$$\log(\mathrm{SFE}) = -1.2729(\pm 0.0242) \times \mu - 9.3275(\pm 0.0128) \quad (16)$$

with an RMSE = 0.37.

Linear fits are performed in 'R' with the package 'HYPERFIT' (Robotham & Obreschkow 2015), which uses traditional likelihood methods to estimate a best-fitting model to multidimensional data, in the presence of parameter covariances, intrinsic scatter, and heteroscedastic errors on individual data points. It assumes that both the intrinsic scatter and uncertainties on individual measurements are Gaussian, and allows for error covariance between orthogonal directions. Hereafter, all the linear fits of this paper are performed

Downloaded from https://academic.oup.com/mnras/article/490/1/868/5569668 by INAF Trieste (Osservatorio Astronomico di Trieste) user on 05 November 2020

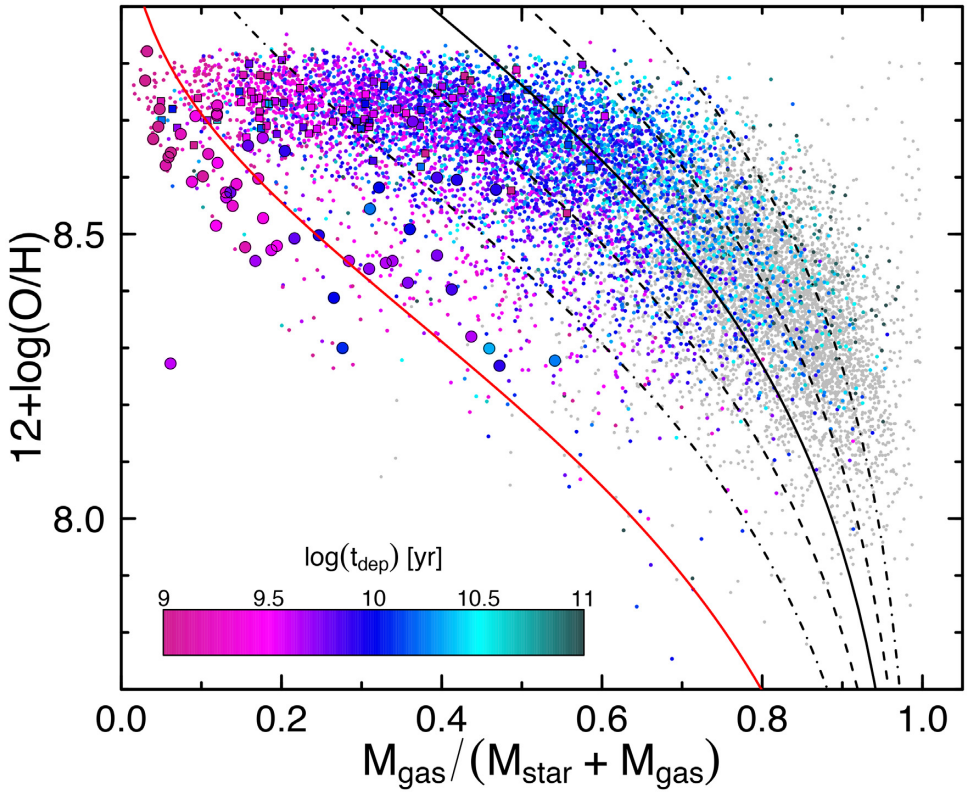

Figure 4. Gas fraction and metallicity relation (μ–Z) as a function of depletion time for all galaxies in our sample. SDSS/AFALFA and SDSS/GASS are shown in dots, SDSS/COLD GASS in filled squares, and Virgo galaxies in large filled circles. Galaxies outside our completeness limit are shown in grey dots. Using equation (2), we are showing an effective yield of 0.01 in solid line, 0.014 and 0.007 in dashed lines, and 0.0047 and 0.021 as dot–dashed lines. The red solid line is the prediction of the closed-box model with oxygen yield $y_0 = 0.002\,68$ (Pilyugin et al. 2004).

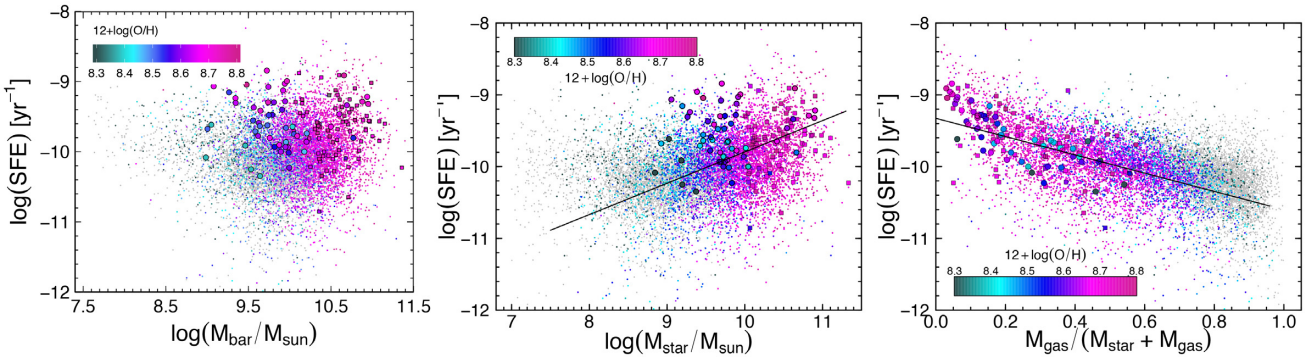

Figure 5. Scaling relationships between the SFE with respect to Baryonic mass (left), stellar mass (centre), and gas fraction (right). All the figures are colour coded as a function of the gas metallicity. Linear fits correspond only to galaxies within the completeness limit, and are given in equations (15) and (16), respectively. The symbols are the same as in Fig. 4.

using HYPERFIT, only to those galaxies within the completeness limit, and taking into account errors in both the axes. As a goodness of fit, we estimate the root mean square error (RMSE; defined as $\sqrt{\sum_{i=1}^{n}(y_i - \hat{y})^2/n}$, where y_i is the i-th observation of y, and $\hat{y}$ is the predicted y value given the model).

Furthermore, we examine the colour excess $E(B-V)_{\rm gas}$ as an indicator of extinction. We find a clear correlation of $E(B-V)_{\rm gas}$ with $M_{\rm bar}$, given by equation (17) where massive galaxies show a higher amount of extinction for $\log(M_{\rm bar}) > 9.5$ M$_\odot$. We find, however, that for galaxies with $\log(M_{\rm bar}) < 9.5$ M$_\odot$, the relationship tends to flatten, with a median value of $E(B-V)_{\rm gas} = 0.15$ (see Fig. 6, top).

$$E(B-V)_{\rm gas} = 0.6861\ (\pm\ 0.0116) \times \log(M_{\rm bar}) - 6.532\ (\pm\ 0.119) \quad (17)$$

with an RMSE = 0.22, for $\log(M_{\rm bar}) > 9.5$.

On the other hand, the SSFR increases linearly with the gas fraction (see Fig. 6, bottom), as expected due to the downsizing effect. Galaxies with very high gas fractions are mostly outside the

Downloaded from https://academic.oup.com/mnras/article/490/1/868/5569668 by INAF Trieste (Osservatorio Astronomico di Trieste) user on 05 November 2020

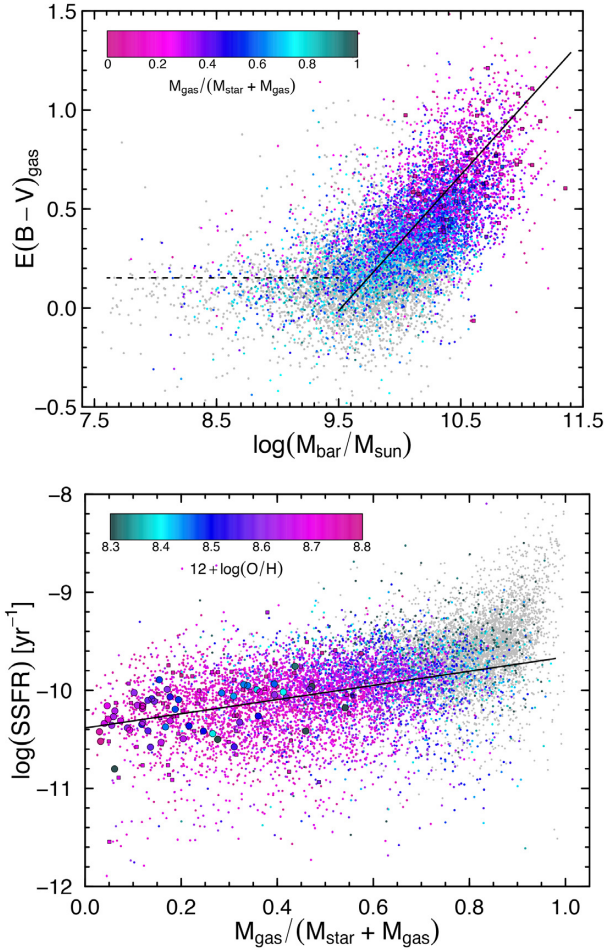

Figure 6. Top: Baryonic mass versus colour excess $E(B-V)$ as a function of gas fraction. Bottom: Gas fraction and SSFR as a function of gas metallicity. Linear fits correspond only to galaxies within the completeness limit, and are given in equations (17) and (18), respectively. All the symbols are similar as in the previous figures.

completeness limits, and show a very steep increase of their SSFR. The linear relation follows the next equation:

$$\log(\mathrm{SSFR}) = 0.7228\ (\pm\ 0.0238) \times \mu - 10.3838\ (\pm\ 0.0126) \quad (18)$$

with an RMSE = 0.37.

In general, galaxies with a high stellar mass tend to convert gas into stars more efficiently, show lower gas fractions, higher metallicities, larger dust content, and a lower SFR per unit mass, consistent with an active star formation history and an earlier assembly of their stellar mass. However, when the baryonic mass is taken as a reference, there is not a single tendency of $M_{\rm bar}$ and SFE, and galaxies with a high $M_{\rm bar}$ show a rather scattered SFE.

On the other hand, galaxies with low stellar mass show exactly the opposite, lower star formation efficiencies, high gas fractions, lower metallicities, a very low dust content, and a high SFR per unit mass. However, galaxies with a low $M_{\rm bar}$ show a scattered anticorrelation with SFE.

We notice a separation between low and massive galaxies only when the baryonic mass is used (Fig. 5, left, and Fig. 6, top). When gas fractions or stellar masses are used as a reference, galaxies will scale uniformly with other properties.

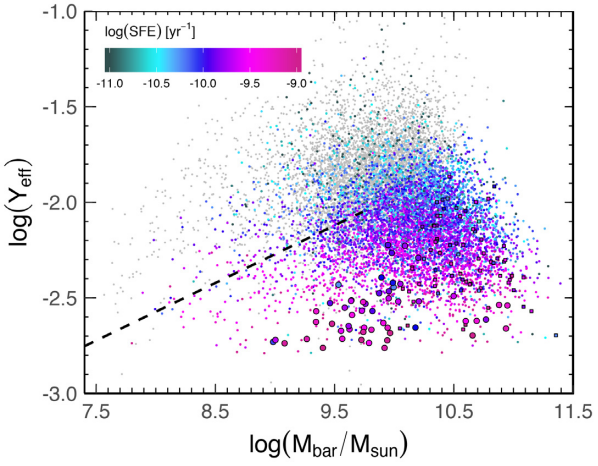

Figure 7. Baryonic mass versus effective oxygen yields colour coded with log(SFE). The dashed line shows the relationship of Ekta & Chengalur (2010) for XMD galaxies (equation 19). All the symbols are similar as in the previous figures.

One of the most interesting relationships we found is between $M_{\rm bar}$ and $y_{\rm eff}$, as shown in Fig. 7. Besides the large dispersion shown in this relationship, we can appreciate a bimodality, when galaxies with $\log(M_{\rm bar}) \lesssim 10$ M$_\odot$ show a correlation, while larger values of M$_{\rm bar}$ show an anticorrelation. This bimodal behaviour is also noticeable for galaxies from the Virgo cluster (large circles in Fig. 7). Furthermore, the $y_{\rm eff}$ seems to scale with SFE, as shown in the colour code of the same figure.

This relationship was previously studied by Ekta & Chengalur (2010) for low-metallicity galaxies. They analysed a set of XMD galaxies, blue compact galaxies, and dwarf irregular galaxies, with metallicities $\leq$1/10 solar. They find that the $y_{\rm eff}$ increases with baryonic mass in their fig. 4 (bottom), which is valid from $7 < \log(M_{\rm bar}) < 9.7$, the corresponding equation to their relation is given by

$$\log(y_{\rm eff})_{\rm Ekta} = 0.301\,16 \times \log(M_{\rm bar}) - 4.9818\,. \quad (19)$$

In Fig. 7, we show the fit of Ekta & Chengalur (2010) in dashed lines, finding a very good agreement with our low mass sample. This strengthens the idea that for $\log(M_{\rm bar}) \lesssim 10$ M$_\odot$, there is a correlation between $M_{\rm bar}$ and $y_{\rm eff}$. Furthermore, other authors have agreed that for low-mass galaxies, $y_{\rm eff}$ correlates with $M_{\rm bar}$ (e.g. Garnett 2002; Tremonti et al. 2004; Lee et al. 2006).

We note that De Rossi et al. (2017) reported a similar behaviour for the $M_{\rm bar}$–$y_{\rm eff}$ relation at $z = 0$ when analysing EAGLE simulations (see their fig. 7). However, in general, these authors obtained lower values of $y_{\rm eff}$, which might be a consequence of a different metallicity calibration, as well as the larger aperture they used to estimate metallicities (30 kpc). Also, in that work, gas fractions were estimated considering only star-forming gas particles inside 30 kpc, while here, we consider the whole gas component within 70 kpc. See Appendix B for more details about aperture effects on the $M_{\rm bar}$–$y_{\rm eff}$ relation in the EAGLE simulations.

From the oxygen yield histogram in Figs 3 and 7, we find that the highest values [$\log(y_{\rm eff}) > -2$] correspond to galaxies with a similar metallicity distribution shown in Fig. 3, but higher gas fractions, with a median of ∼0.7, almost 0.2 dex higher than the general gas fraction distribution in Fig. 3. It is been suggested by Vincenzo et al. (2016) that high values of effective yield may be

Downloaded from https://academic.oup.com/mnras/article/490/1/868/5569668 by INAF Trieste (Osservatorio Astronomico di Trieste) user on 05 November 2020

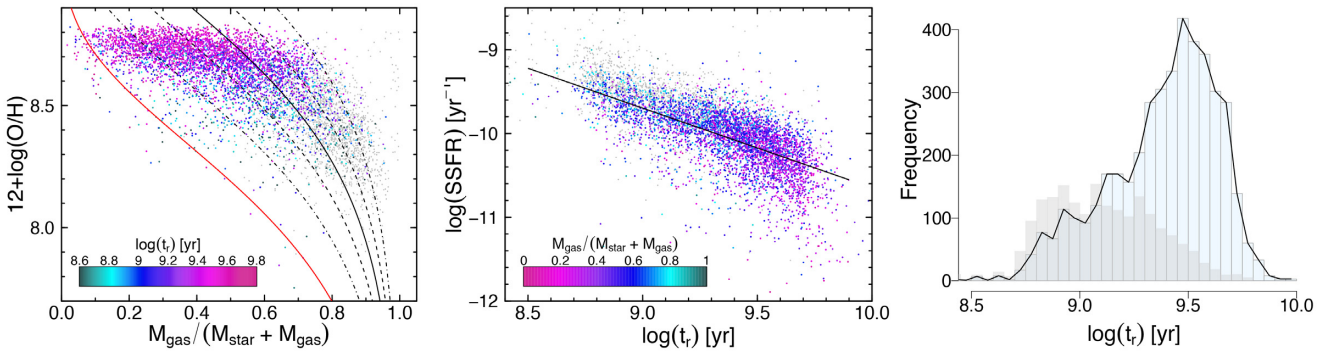

Figure 8. Left: μ–Z relation as a function of age weighted by r-luminosity (t_r). Centre: t_r–SSFR relation as a function of gas fraction. Right: Age histogram. Galaxies within the completeness limit are colour coded (4266 galaxies), while galaxies outside the completeness limit with an stellar age measured are shown in grey (1888 galaxies).

indicative of an IMF favouring massive stars (see also Mollá et al. 2015).

In order to understand the suggested bimodality of the $M_{\rm bar}$–$y_{\rm eff}$ relation in Fig. 7, we will now examine the stellar ages of our galaxies and perform a more detailed analysis of this relationship with more dimensions (Section 6). Furthermore, we seek different scenarios and the feedback processes that can produce such a bimodality by investigating the results from the EAGLE simulations (Section 4).

3.1 Stellar ages

The stellar age in galaxies is key to understand the time-scales in which galaxies have converted their gas into stars. We use the Bayesian-likelihood estimates of the r-band light-weighted ages (t_r) for the SDSS-DR7 estimated by Gallazzi et al. (2005). In summary, the stellar ages are derived by comparing the spectrum of each galaxy to a library of Bruzual & Charlot (2003) models at medium-high spectral resolution, encompassing the full range of physically plausible star formation histories. Similarly to Kauffmann et al. (2003a), they adopted a Bayesian approach to derive a posteriori likelihood distribution of each physical parameter by computing the goodness of fit of the observed spectrum for all the models in the library.

After matching the stellar ages catalogue with the SDSS/ALFALFA SF sample, we obtained 4266 galaxies within the completeness limit and 1888 galaxies outside the completeness limit. The stellar ages are distributed from $\sim 10^{8.6}$ to $10^{9.9}$ yr (see Fig. 8, right), with a negative skew that could be indicative of a second, younger population. We show the μ–Z relation as a function of stellar age (Fig. 8, left); as appreciated, a large fraction of the galaxies have high gas metallicities. Additionally, we find that the t_r–SSFR relation is tightly anticorrelated, and we have included this relationship as it may be useful to have a rough estimate of the stellar age when it cannot be estimated through more sophisticated methods. The obtained fit is

$$\log(\mathrm{SSFR}) = -0.9509\ (\pm\ 0.0156)\times\log(t_r) - 1.1391\ (\pm\ 0.1462)\,, \quad (20)$$

with an RMSE = 0.29.

A further discussion on the implication of the stellar age is given in Section 6.

4 CONFRONTING SIMULATIONS WITH OBSERVATIONS

In order to get some insight into the astrophysical processes that could drive the observed scaling relations for $y_{\rm eff}$, we compared our results with predictions from the EAGLE suite of cosmological simulations (Crain et al. 2015; Schaye et al. 2015).[3] In Section 4.1, we briefly describe the set of EAGLE simulations used in this work and the simulated galaxy sample. A comparison between observational data and EAGLE results is presented in Section 4.2, while in Section 4.3 we discuss the effect of AGN feedback on effective yields.

4.1 EAGLE simulations

EAGLE simulations were performed by using a modified version of the GADGET-3 hydrodynamical code (Springel 2005). These simulations track the joint evolution of dark matter and baryons within different periodic comoving volumes, adopting different resolutions. The cosmology used by EAGLE is $H_0 = 67.77\ \mathrm{km\,s^{-1}\,Mpc^{-1}}$, $\Omega_{\rm M} = 0.307$, and $\Omega_\Lambda = 0.693$. Different processes are included in the EAGLE subgrid physical model, such as radiative cooling and heating of the gas, star formation, chemical enrichment, stellar and AGN feedback, among others (see Schaye et al. 2015; Crain et al. 2015, for more details).

Here, we will focus on the analysis of the so-called Recal-L025N0752, Ref-L050N0752, AGNdT9-L050N0752, and NO-AGN-L050N0752 simulations, as they provide important clues for the understanding of the observed $y_{\rm eff}$ trends (see below). The suffix in the name of the simulations indicates the box length in comoving megaparsec (cMpc, e.g. L025) and the cube root of the initial number of particles per species (e.g. N0752). For simulations run with the reference model (denoted with the prefix 'Ref'), the subgrid parameters associated with energy feedback were calibrated to obtain good agreement with the $z = 0.1$ galaxy stellar mass function (GSMF), while also reproducing the observed sizes of present-day disc galaxies. Higher resolution simulations (e.g. Recal-L025N0752) implement also a 'Recal-' model, which uses subgrid parameters that have been recalibrated to improve the fit to the $z \sim 0$ GSMF when increasing the resolution. Variations of AGN

[3] See http://eagle.strw.leidenuniv.nl and http://www.eaglesim.org/ for different data products, images, and movies (McAlpine et al. 2016; The EAGLE team 2017).

Downloaded from https://academic.oup.com/mnras/article/490/1/868/5569668 by INAF Trieste (Osservatorio Astronomico di Trieste) user on 05 November 2020

feedback parameters have only been explored within comoving volumes of side lengths of 50 cMpc ('L050' runs); thus, the latter simulations will be used to study the impact of AGN feedback on $y_{\rm eff}$. In particular, simulation AGNdT9-L050N0752 assumes a temperature increment associated with AGN heating of $\Delta T_{\rm AGN} = 10^9$ K while, for the reference model, $\Delta T_{\rm AGN} = 10^{8.5}$ K. Increasing $\Delta T_{\rm AGN}$ drives more energetic individual feedback events, generally leading to smaller radiative losses in the ISM. Larger values of $\Delta T_{\rm AGN}$ produce a more intermittent feedback process (see De Rossi et al. 2017, for a deep analysis of AGN feedback effects on the global chemical enrichment of galaxies). In the case of the simulation NO-AGN-L050N0752, the black hole (BH) model is turned off: BH gas accretion and AGN feedback are completely disabled.

Throughout this work, the global properties of simulated galaxies that are typically measured from optical diagnostics (e.g. $M_{\rm star}$, SFRs, stellar ages, chemical abundances) are estimated considering bound particles within a spherical aperture of radius 30 kpc centred on the potential minimum of the system. According to Schaye et al. (2015), stellar masses derived in this way are comparable to those obtained within a projected circular aperture of the Petrosian radius. As oxygen abundances are typically inferred from SF gas H II regions, in this work, we evaluate chemical abundances taking into account only *star-forming* gas particles, similarly to the procedure applied by De Rossi et al. (2017). In Appendix B, we show that the main trends found for EAGLE-simulated yields are robust against aperture effects.

For estimating gas masses ($M_{\rm gas}$), we follow Crain et al. (2017) and consider a larger aperture of 70 kpc, which roughly corresponds to the Arecibo *L*-Band Feed Array (ALFA) full width at half-maximum (FWHM) beam size of ∼3.5 arcmin (Giovanelli et al. 2005) at the median redshift of the GASS sample, $z = 0.037$ (Catinella et al. 2010). In the case of simulations, we define $M_{\rm gas}$ as the total hydrogen mass enclosed by 70 kpc. We have checked that, for the scaling relations studied here, similar general trends are obtained if defining $M_{\rm gas}$ as the neutral hydrogen mass ($M_{\rm Hn}$), where $M_{\rm Hn}$ was calculated following previous works (e.g. Marasco et al. 2016). As the estimate of $M_{\rm Hn}$ involves further assumptions and approximations, for the sake of simplicity, we have not applied such separation in this work. The larger aperture of 70 kpc used for estimating $M_{\rm gas}$ leads to ≈0.1 higher gas fractions than those obtained if using an aperture of 30 kpc. As we will show in Appendix B, if we measure all simulated quantities within 30 kpc, only moderate changes are obtained in the normalization and scatter of the $M_{\rm bar}$–$y_{\rm eff}$ relation but the main trends are preserved.

Finally, to avoid resolution issues, in our analysis we only consider the simulated galaxies with $M_{\rm star} \geq 10^9$ M$_\odot$ (Schaye et al. 2015). Unless otherwise specified, we only present results for galaxies with $M_{\rm star} \geq 10^9$ M$_\odot$.

4.2 Comparison with observations

Within the EAGLE suite of simulations, the high-resolution Recal-L025N0752 run shows the best agreement with the observed metallicity scaling relations (e.g. Schaye et al. 2015; De Rossi et al. 2017, 2018). In particular, De Rossi et al. (2017) found that these simulations are able to reproduce the observed trends for the mass–metallicity relation and its secondary dependences on gas fraction, SFR, SSFR, and stellar age. Regarding effective yields, the Recal-L025N0752 run also predicts effective yields consistent with observations of local low-mass galaxies (see De Rossi et al. 2017, Fig. 7), but, at higher masses, $y_{\rm eff}$ tends to decrease with mass, departing from the observed behaviour reported by Tremonti et al. (2004). It is worth noting that De Rossi et al. (2017) estimated gas masses considering SF gas particles within 30 kpc and such a definition is different to that applied here (Section 4.1). So, caution should be taken when comparing our results with those obtained by De Rossi et al. (2017). Tremonti et al. (2004) derived gas masses indirectly from the observed SFRs assuming a Schmidt law (Kennicutt 1998). We will show that effective yields obtained from the Recal-L025N0752 simulations and observational results presented here are in better agreement over a larger mass range.

As a sanity check, in Fig. 9 we show a direct comparison between our main ALFALFA/SDSS sample, and the result of the high-resolution EAGLE simulations. Simulations and observations are in a perfect agreement. Furthermore, even the dispersion in the scaling relations is recovered, where the $M_{\rm bar}$–$y_{\rm eff}$ relation shows a bimodal behaviour, and the $t_{\rm r}$–SSFR relation shows a very tight anticorrelation. We only note that EAGLE galaxies tend to be older than observed ones, which might be a consequence of the lower mass cut that we imposed on our simulated sample ($M_{\rm star} \geq 10^9$ M$_\odot$).

In order that simulated galaxies are well resolved and to avoid numerical artefacts, we follow De Rossi et al. (2017) and analyse only galaxies with $M_{\rm star} > 10^9$ M$_\odot$ (see also Schaye et al. 2015). With this mass limit, we obtain, for example, more than 7000 baryonic particles within an aperture of 30 kpc for the Recal-L025N0752 simulation. We note, however, that this lower mass cut is below the mass limit associated with the observed sample within the completeness limit ($>10^7$ M$_\odot$, Fig. 2). Had we included in our analysis the subsample of simulated galaxies with 10^7 M$_\odot$ $< M_{\rm star} < 10^9$ M$_\odot$, higher effective yields would have been obtained at the low-mass end of our analysed scaling relations, reaching $\log(y_{\rm eff}) \sim -1$ in some cases. The increase of $\log(y_{\rm eff})$ is explained considering that galaxies within such a low mass range tend to show higher than average gas fractions and SSFRs, and lower than average SFEs and ages (see Fig. 10). Finally, we note that a mass limit of 10^7 M$_\odot$ selects systems poorly resolved (less than 50 baryonic particles within 30 kpc) even for the Recal-L025N0752 simulation (the higher resolution simulation within the EAGLE suite). Therefore, we decided to apply a cut at a higher mass (10^9 M$_\odot$).

We also notice that high values of $y_{\rm eff} \gtrsim -1.8$ (over solar) are predicted for simulated gas-rich galaxies with the lowest SFE, highest SSFR, and youngest ages.

4.3 Impact of AGN feedback

The third panel in Fig. 9 shows that observations and simulations predict a correlation between $y_{\rm eff}$ and $M_{\rm bar}$ at low masses. This behaviour has been previously explained in the literature by invoking the higher efficiency of galactic winds to eject metals from the shallower potential wells of low-mass galaxies. On the other hand, at high masses, a flattening of the $M_{\rm bar}$–$y_{\rm eff}$ relation was reported by Tremonti et al. (2004). Interestingly, our main ALFALFA/SDSS and EAGLE samples predict an anticorrelation between $y_{\rm eff}$ and $M_{\rm bar}$ for massive galaxies. It is important to note that Tremonti et al. (2004) used indirect estimations of gas masses, while in this work we are using direct measurements. In this section, we will show that such an effect seems to be a consequence of AGN feedback.

Fig. 10 shows effective yields as a function of baryonic mass for different EAGLE simulations: Recal-L025N0752, Ref-L050N0752, AGNdT9-L050N0752, and NO-AGN-L050N0752 (from top to bottom, as indicated in the figure). Median relations at $z = 0$ are shown binned in $\mu = M_{\rm gas}/(M_{\rm gas} + M_{\rm star})$, SFE, SSFR, and stellar mean age (from left to right, as indicated in the figure).

Downloaded from https://academic.oup.com/mnras/article/490/1/868/5569668 by INAF Trieste (Osservatorio Astronomico di Trieste) user on 05 November 2020

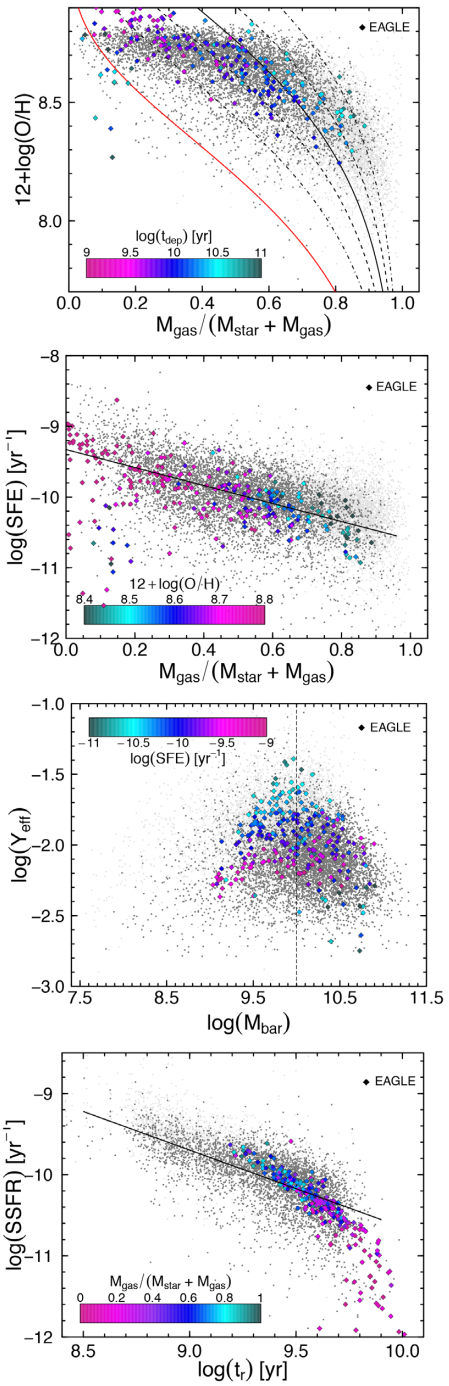

Figure 9. From top to bottom: μ–Z, μ–SFE, $M_{\rm bar}$–$y_{\rm eff}$, and $t_{\rm r}$–SSFR relations. The EAGLE high-resolution simulations corresponding to Recal-L025N0752 are shown in diamonds, colour coded as the variable in the inset colour bar. The dark-grey dots show our main ALFALFA/SDSS sample within the completeness limit, while the light-grey dots show galaxies outside the completeness limit. The fits shown in solid lines for the 2nd and 4th panels, from top to bottom, correspond to equations (16) and (20), respectively.

All considered mass bins contain $N_{\rm bin} \geq 5$ galaxies; less populated bins ($5 \leq N_{\rm bin} < 10$) are marked with a circle. For simulation Recal-L025N0752, stellar mean age is weighted by luminosity in the r band using photometric data of stellar particles available in the public EAGLE data base (McAlpine et al. 2016). As photometric data are not available for all 'L050N0752' simulations, we use the mass-weighted mean ages ($t_{\rm m}$) when analysing samples of galaxies extracted from those simulations.

The top panels in Fig. 10 show results for the Recal-L025N0752 simulation. In each panel, the black solid line depicts the median relation associated with the whole sample of galaxies. It is clear that, for smaller galaxies, $y_{\rm eff}$ seems to correlate with $M_{\rm bar}$, on average. In addition, at a given $\log(M_{\rm bar}) \lesssim 10$ M$_\odot$, systems with lower values of $y_{\rm eff}$ show lower $f_{\rm gas}$, higher SFEs, and lower SSFRs, but there is a no clear dependence of $y_{\rm eff}$ on age at low masses. On the other hand, for more massive galaxies, $y_{\rm eff}$ decreases with $M_{\rm bar}$ on average. In addition, at a given $\log(M_{\rm bar}) \gtrsim 10$ M$_\odot$, lower values of $y_{\rm eff}$ are associated with old galaxies with low gas fractions, SFEs, and SSFRs; thus, galaxies whose star-forming process is being quenched.

In order to investigate at what extent AGN feedback might be responsible for the very low values of $y_{\rm eff}$ at high masses, we analyse simulations Ref-, AGNdT9-, and NO-AGN-L050N0752. As mentioned, the 'Ref' model is the standard one, while the 'NO-AGN' model suppresses all AGN feedback effects. On the other hand, the 'AGNdT9' model predicts a stronger impact of AGN feedback on the chemical evolution of galaxies, as discussed in detail in De Rossi et al. 2017 (see their sections 3.3 and 7.1.2). The three lower rows of panels in Fig. 10 compare the $M_{\rm bar}$–$y_{\rm eff}$ relations for the aforementioned simulations. It is clear that, at low masses, similar trends are obtained for the different AGN feedback prescriptions. As expected, low-mass systems seem not to be significantly affected by AGN feedback. However, as mass increases, AGN feedback effects seem to be stronger, leading to an anticorrelation between $y_{\rm eff}$ and $M_{\rm bar}$ at the high-mass end. Simulations run with the 'Ref' and 'AGN-dT9' model, which include AGN feedback, predict such anticorrelation, while the 'NO-AGN' model, in which all BH processes were turned off, predicts a *correlation* between $y_{\rm eff}$ and $M_{\rm bar}$ at high masses. Moreover, the simulation 'AGN-dT9', which implements a higher temperature increment associated with AGN heating ($\Delta T_{\rm AGN} = 10^9$ K), leads to a stronger decrease of $y_{\rm eff}$ at high masses. According to our results, systems more affected by AGN feedback are old and exhibit very low $y_{\rm eff}$, μ, SFE, and SFR. Thus, AGN feedback seems to have quenched their SF and chemical evolution. Only gas-rich mergers or significant gas accretion events might lead to further evolution of such galaxies.

Our findings for massive galaxies are consistent with previous results by De Rossi et al. (2017). According to these authors, at a given mass, SFR tends to decrease as $\Delta T_{\rm AGN}$ increases because the less frequent but more energetic feedback events corresponding to a higher $\Delta T_{\rm AGN}$ are more efficient at regulating SFR in massive galaxies. In addition, at a given mass, a higher $\Delta T_{\rm AGN}$ leads to lower metallicity values. De Rossi et al. (2017) conclude that this behaviour seems to be driven by AGN feedback through three different channels: the ejection of metal-enriched material, which generates a net metal depletion in simulated galaxies; the heating of gas remaining in galaxies, which quenches the SF activity and, thus, prevents further chemical enrichment from star formation; and a minor role of net metal dilution after star formation is suppressed by AGNs.

Downloaded from https://academic.oup.com/mnras/article/490/1/868/5569668 by INAF Trieste (Osservatorio Astronomico di Trieste) user on 05 November 2020

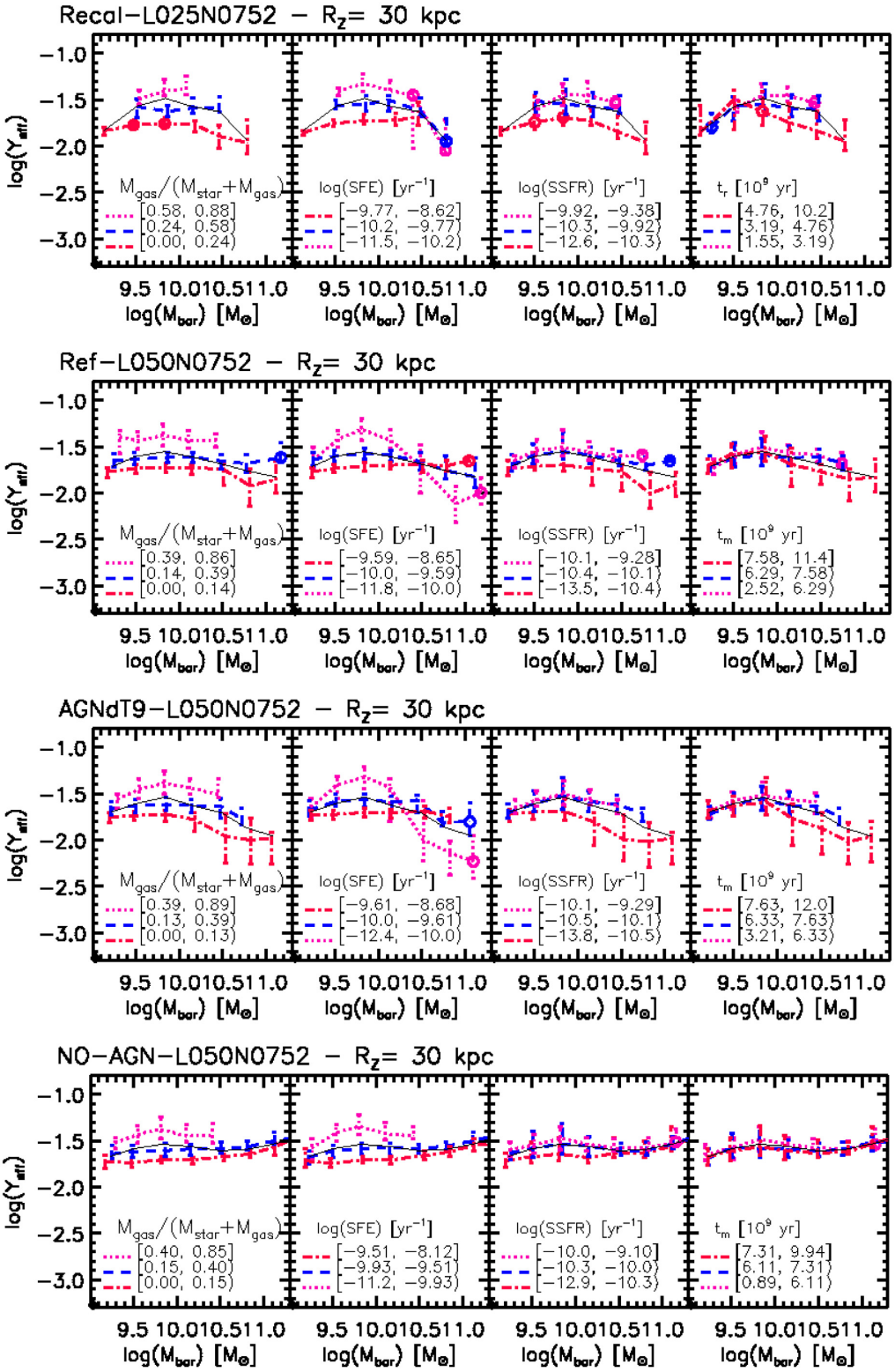

Figure 10. Effective yields as a function of baryonic mass for different EAGLE simulations: Recal-L025N0752, Ref-L050N0752, AGNdT9-L050N0752, and NO-AGN-L050N0752 (from top to bottom, as indicated in the figure). The curves with error bars indicate the $z = 0$ median relations together with the 25th and 75th percentiles corresponding to simulated galaxies binned in $f_{\rm gas} = M_{\rm gas}/(M_{\rm gas} + M_{\rm star})$, SFE, SSFR, and stellar mean age (from left to right, as indicated in the figure). All considered mass bins contain $N_{\rm bin} \geq 5$ galaxies; less populated bins ($5 \leq N_{\rm bin} < 10$) are marked with a circle. As a reference, the median relation associated with the whole sample of galaxies is shown with a black solid curve in each panel. Yields in this figure were derived by measuring metallicities inside an aperture of $R_Z = 30$ kpc. See Appendix B, for an analysis of aperture effects.

Downloaded from https://academic.oup.com/mnras/article/490/1/868/5569668 by INAF Trieste (Osservatorio Astronomico di Trieste) user on 05 November 2020

5 ON THE RELATIONSHIP BETWEEN $M_{\rm BAR}$ AND $y_{\rm EFF}$

With the aim of characterizing the driver of the opposite trends between low- and high-$M_{\rm bar}$ galaxies, we analyse in more detail the $M_{\rm bar}$–$y_{\rm eff}$ relation for different cuts in SFE, colour coded by age, as shown in Fig. 11. From top left to bottom right, all the black linear and polynomial fits from Fig. 11 are shown in equation (21), with its respective RMSE. The dashed lines in panels (d) and (e) show the fit of Ekta for XMD galaxies (equation 19), while the vertical dashed lines in panels (d) and (e) show the inflection point (stellar mass of the maximum value of the fitted function), in which the data change from a correlation to an anticorrelation, $\log(M_{\rm bar}) \sim 10.2$ for panel (d), and $\log(M_{\rm bar}) \sim 10.3$ for panel (e).

$$\log(y_{\rm eff}) = -0.5013(\pm0.0559) \times \log(M_{\rm bar}) + 3.134(\pm0.5769)$$

$$\text{for } \log(\text{SFE}) < -10.4, \text{ with RMSE} = 0.25$$

$$\log(y_{\rm eff}) = -0.4663(\pm0.0546) \times \log(M_{\rm bar}) + 2.732(\pm0.5626)$$

$$\text{for } -10.4 < \log(\text{SFE}) < -10.1, \text{ with RMSE} = 0.24$$

$$\log(y_{\rm eff}) = -0.069\,96(\pm0.133\,71) \times \log(M_{\rm bar}) + 2.842(\pm1.373)$$

$$\text{for } -10.1 < \log(\text{SFE}) < -9.8, \text{ with RMSE} = 0.16$$

$$\log(y_{\rm eff}) = 47.4476(\pm17.1622) - 16.3741(\pm5.2340) \times \log(M_{\rm bar})$$

$$+ 1.7786(\pm0.5309) \times \log(M_{\rm bar})^2 - 0.0638(\pm0.0179) \times \log(M_{\rm bar})^3$$

$$\text{for } -9.8 < \log(\text{SFE}) < -9.5, \text{ with RMSE} = 0.13$$

$$\log(y_{\rm eff}) = 34.9975(\pm17.3501) - 12.5641(\pm5.3152) \times \log(M_{\rm bar})$$

$$+ 1.3836(\pm0.5414) \times \log(M_{\rm bar})^2 - 0.0501(\pm0.0183) \times \log(M_{\rm bar})^3$$

$$\text{for } -9.5 < \log(\text{SFE}), \text{ with RMSE} = 0.14\,. \quad (21)$$

For a comparison, we are including as well the EAGLE simulation model 'Recal' in green lines, and 'NO-AGN' in orange dot–dashed lines. The simulations shown in each panel correspond to the closest SFE from the models. Panels (a) and (b) show the simulation 'Recal' with log(SFE) in the range [−11.5, −10.2], panel (c) in the range [−10.2, −9.7], and panels (d) and (e) show the range [−9.7, −8.62]. As for the 'NO-AGN' simulation, panels (a), (b), and (c) show log(SFE) in the range [−11.2, −9.93], panel (d) shows the range [−9.93, −9.51], and panel (e) the range [−9.51, −8.12].

From Fig. 11, panels (a) and (b) show a clear anticorrelation between $M_{\rm bar}$ and $y_{\rm eff}$. Furthermore, galaxies with such lower values of SFE are dominated mostly by old galaxies. Both the panels have a median age of $\log(t_{\rm r}) \sim 9.5$. The EAGLE simulations show as well an anticorrelation in both the 'Recal' and 'NO-AGN' models for the same panels. What we could conclude is that for older galaxies the effective yield will decrease as the baryonic mass increases.

For galaxies with $-10.1 < \log(\text{SFE}) < -9.8$ (panel c), there is no clear tendency; the median age for them is $\log(t_{\rm r}) \sim 9.4$, and corresponds to a rather transitional stage of galaxies. The next panels, (d) and (e), show intervals with a higher SFE, and show a relation for $\log(M_{\rm bar}) < 10$, which anticorrelates for higher baryonic masses. Galaxies with $\log(M_{\rm bar}) > 10$ are clearly older galaxies with median $\log(t_{\rm r}) \sim 9.4$ and 9.3 for panels (d) and (e), respectively. Contrary, galaxies with $\log(M_{\rm bar}) < 10$ are young galaxies with median $\log(t_{\rm r}) \sim 9.1$ and 9.0 for panels (d) and (e), respectively. The simulation 'Recal' agrees with a correlation for lower baryonic masses; however, it does not show any values for higher masses because of its limited associated simulated box (25 cMpc side length). On the other hand, the 'NO-AGN' model shows that the correlation would continue for more massive galaxies if galaxies had not experience any AGN activity in their history.

From this figure, we can deduce that galaxies that are converting their gas into stars less efficiently [e.g. $\log(\text{SFE}) < -10.4$] are older, and show a clear anticorrelation between their oxygen yield and baryonic mass. On the other hand, galaxies that are efficient at converting their mass into stars [e.g. $\log(\text{SFE}) > -9.8$] show a bimodality that is separated by age, in which the yield increases with $M_{\rm bar}$ for younger galaxies up to $\log(M_{\rm bar}) < 10$, and decreases for older galaxies for $\log(M_{\rm bar}) > 10$.

Since the stellar age is one of the key properties in our scaling relations, in Fig. 12 we show the $M_{\rm bar}$–$y_{\rm eff}$ relation for different cuts of age, colour coded by their depletion time. All the symbols are similar to the previous figure. As a comparison, we are showing as well the Recal and NO-AGN simulations in green and orange lines, respectively. Panel (c) shows the 'Recal' simulation for the age range of [9.19, 9.5] yr, panel (d) for [9.5, 9.67] yr, and panel (e) for [9.67, 10], respectively. Unfortunately, the EAGLE simulations do not have a high enough resolution to appropriately describe younger, low-mass galaxies, for which panels (a) and (b) do not show any simulations. On the other hand, the 'NO-AGN' model for an age range of [8.9, 9.78] is shown in panels (b), (c), and (d), while panel (e) shows the age range [9.78, 9.86]. Similarly to the 'Recal' simulations, the resolution is not good enough to describe younger low-mass galaxies. The fits to the observational data for the $M_{\rm bar}$–$y_{\rm eff}$ relation in bins of age (Fig. 12) are listed below:

$$\log(y_{\rm eff}) = 0.2217(\pm0.0366) \times \log(M_{\rm bar}) - 4.339(\pm0.363)$$

$$\text{for } \log(t_{\rm r}) < 8.9, \text{ with RMSE} = 0.23$$

$$\log(y_{\rm eff}) = 0.1515(\pm0.0196) \times \log(M_{\rm bar}) - 3.672(\pm0.197)$$

$$\text{for } 8.9 < \log(t_{\rm r}) < 9.2, \text{ with RMSE} = 0.22$$

$$\log(y_{\rm eff}) = 0.099\,63(\pm0.033\,03) \times \log(M_{\rm bar}) - 3.168(\pm0.337)$$

$$\text{for } 9.2 < \log(t_{\rm r}) < 9.4 \text{ with RMSE} = 0.21$$

$$\log(y_{\rm eff}) = -0.4195(\pm0.0399) \times \log(M_{\rm bar}) + 2.186(\pm0.414)$$

$$\text{for } 9.4 < \log(t_{\rm r}) < 9.6 \text{ with RMSE} = 0.21$$

$$\log(y_{\rm eff}) = -0.4532(\pm0.0539) \times \log(M_{\rm bar}) + 2.553(\pm0.567)$$

$$\text{for } 9.6 < \log(t_{\rm r}) \text{ with RMSE} = 0.21\,. \quad (22)$$

In Fig. 12, the stellar age provides a clear separation between the correlation and anticorrelations of the $M_{\rm bar}$–$y_{\rm eff}$ relation. For galaxies with a $\log(t_{\rm r}) < 8.9$, there is a clear correlation between those variables, the depletion times, i.e. the conversion of gas into stars is fast, and there is a very good agreement with the Ekta & Chengalur (2010) sample for XMD galaxies. The next panels (b) and (c) show how this correlation starts to flatten. For the same panels, the simulations 'Recal' and 'NO-AGN' show a similar tendency with a somehow higher yield. For panels (d) and (e), we have an anticorrelation, in which the $y_{\rm eff}$ decreases as $M_{\rm bar}$ increases. Furthermore, the depletion times increase with age, with a median $\log(t_{\rm r})$ of 9.6, 9.8, 9.9, 9.97, and 10.1 for panels (a)–(e), respectively. The 'Recal' simulation (green line) for panel (e) agrees quite well with the observations. Again, the model for 'NO-AGN' shows how

Downloaded from https://academic.oup.com/mnras/article/490/1/868/5569668 by INAF Trieste (Osservatorio Astronomico di Trieste) user on 05 November 2020

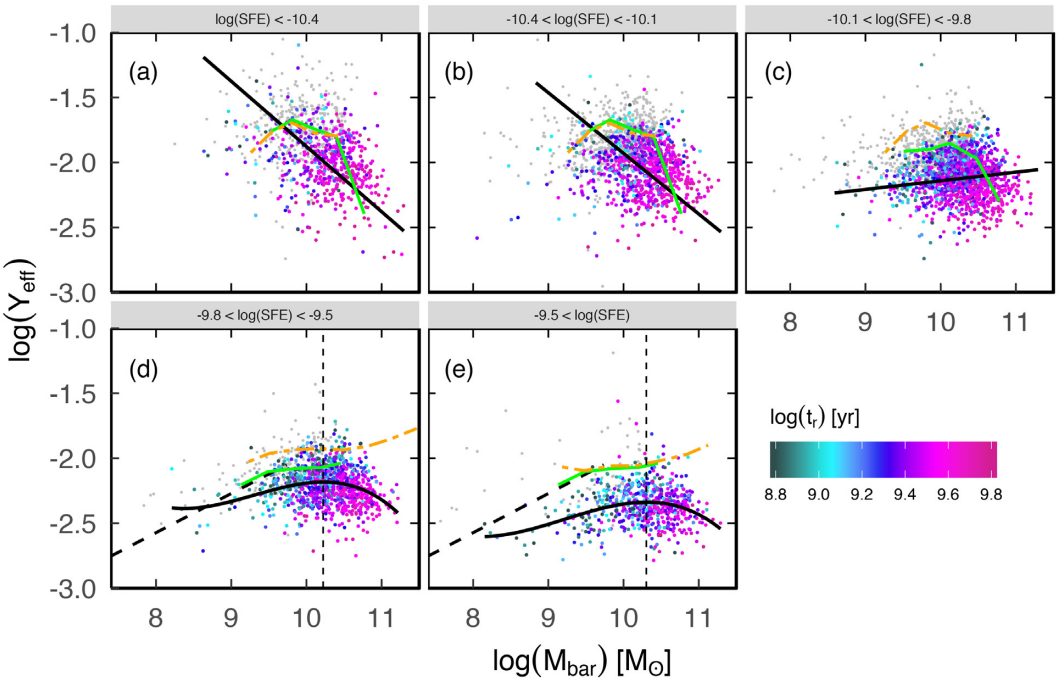

Figure 11. Baryonic mass as a function of effective oxygen yield divided in panels of SFE. Every panel is colour coded by age using a common colour scale shown in the bottom right panel. The black solid lines show the linear and third-order polynomial fit to each panel, respectively, with its respective equations given in equation (21). The solid green lines correspond to the Recal-L025N0752 simulations of Fig. 10 for the same variables. The dot dashed orange lines correspond to the No-AGN-L050N0752 models from the same figure. The dashed black line corresponds to the relation of Ekta & Chengalur (2010) for XMD galaxies (equation 19). The vertical dashed lines show the point of inflection $\log(M_{\rm bar}) \sim 10.22$ for panel (d), and $\log(M_{\rm bar}) \sim 10.3$ for panel (e). Only galaxies from the SDSS and ALFALFA surveys with measured age are shown (4266 galaxies).

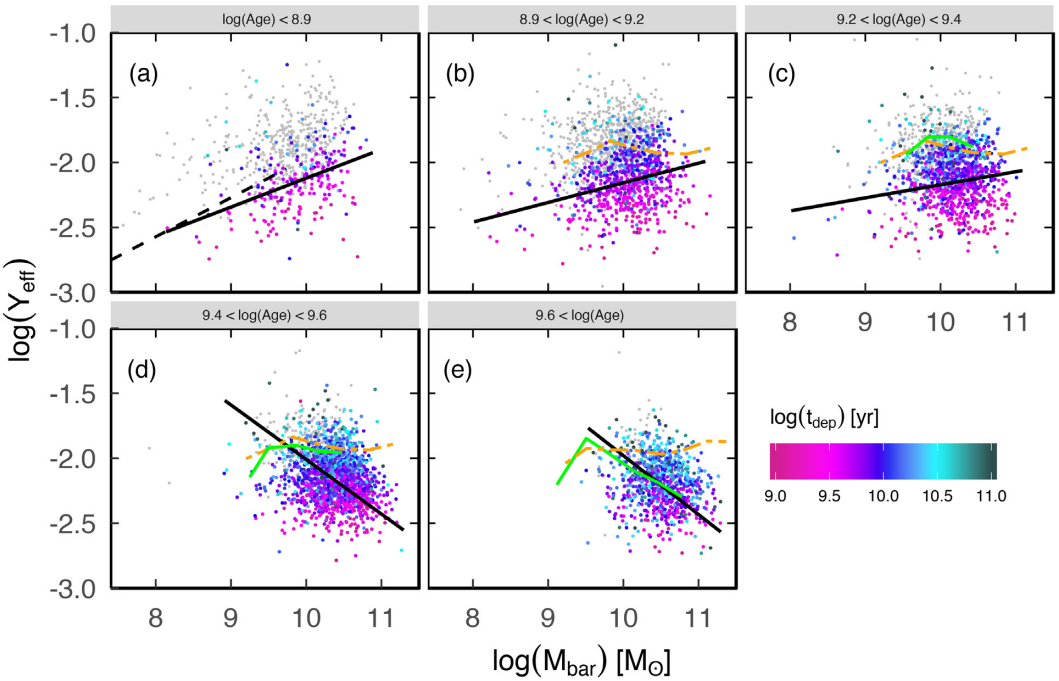

Figure 12. Baryonic mass as a function of effective oxygen yield divided in panels of age. Every panel is colour coded with $\log(t_{\rm dep})$ using a common colour scale shown in the bottom right panel. The black solid lines show the linear fit to each panel, with its respective equations given in equation (22). The solid green lines correspond to the Recal-L025N0752 simulations of Fig. 10 for the same variables. The dot dashed orange lines correspond to the No-AGN-L050N0752 models from the same figure. The dashed black line corresponds to the relation of Ekta & Chengalur (2010) for XMD galaxies (equation 19).

Downloaded from https://academic.oup.com/mnras/article/490/1/868/5569668 by INAF Trieste (Osservatorio Astronomico di Trieste) user on 05 November 2020

the $M_{\rm bar}$–$y_{\rm eff}$ relation would continue to increase when no AGN is present in their history.

6 DISCUSSION

The mass of a galaxy is critical for the fate of its evolution. Stars in more massive galaxies tend to have formed earlier and over shorter time-scales, contrary to stars in low-mass galaxies, which formed later and on longer time-scales. Recently, the interest in this well-established observational result has grown, and its implications have been more and more appreciated. This downsizing effect (e.g. Thomas et al. 2005; Noeske et al. 2007; Fontanot et al. 2009) is still a matter of several studies. Indeed, a downsizing effect is invoked to explain the differences between opposite mass population of galaxies; however, its nature and physical explanation still remain unclear (e.g. Neistein, van den Bosch & Dekel 2006).

Several authors have explored the properties of galaxies of opposite masses, for instance, Kauffmann et al. (2003c) show that low-redshift galaxies divide into two distinct families at a stellar mass of 3×10^{10} $M_{\odot}$. Lower mass galaxies have young stellar populations and low surface mass densities. A significant fraction of them have experienced recent starbursts, and the efficiency of the conversion of baryons into stars in low-mass galaxies increases in proportion to halo mass, perhaps as a result of supernova feedback processes. At stellar masses above 3×10^{10} $M_{\odot}$, there is a rapidly increasing fraction of galaxies with old stellar populations, high surface mass densities, and the high concentrations typical of bulges. They suggest that the SFE decreases in the highest mass haloes, and that little star formation occurs in massive galaxies after they have assembled.

Furthermore, by analysing the H I and H2 content in galaxies, Saintonge et al. (2011) found that for high-mass galaxies, the molecular and atomic gas depletion time-scales are comparable, but in low-mass galaxies, molecular gas is being consumed much more quickly than atomic gas. Furthermore, scaling relations such as the *M*–SSFR (e.g. Noeske et al. 2007) clearly show that low-mass galaxies are actively forming stars at a higher rate than massive galaxies per unit mass.

In is worth nothing that, in comparison with previous works that divide galaxies into two distinct families based on their stellar mass, we find that the stellar age is a more clear divider in the properties of galaxies.

Most of the scaling relations analysed in this paper show smooth relations or anticorrelations, with RMSE values around 0.22 [$M_{\rm bar} - E(B-V)_{\rm gas}$, Fig. 6], RMSE = 0.29 ($t_{\rm r}$–SSFR, Fig. 8), and RMSE > 0.3 (e.g. $M_{\rm star}$–SFE, Fig. 5). On the other hand, the $M_{\rm bar}$–$y_{\rm eff}$ relationship (Fig. 12) shows a clear bimodal behaviour when galaxies are separated by (i) stellar age, with RMSE values going from 0.21 to 0.23, and (ii) by SFE (Fig. 11), with RMSE values from 0.14 to 0.25.

Fig. 12 offers a clear picture of how galaxies are evolving. For one hand, young galaxies show faster depletion times, and a clear correlation between $M_{\rm bar}$ and $y_{\rm eff}$. This behaviour has also been observed by several authors, for instance, Thuan et al. (2016) analysed as well the $M_{\rm bar}$–$y_{\rm eff}$ relation for BCD galaxies, finding a very similar result (see fig. 13 of their paper), where there is a correlation for $\log(M_{\rm bar}) < 10$ $M_{\odot}$, which disappears at higher $M_{\rm bar}$, although suggesting a possible anticorrelation for higher masses that is not clear due to a low statistic. Similarly, other authors have analysed this relation for low-mass/metallicity galaxies, showing a very similar correlation (e.g. Garnett 2002; Ekta & Chengalur 2010).

Among the possible explanations of why the effective yield increases with baryonic mass, it has been argued by Garnett (2002), Tremonti et al. (2004), and Silich & Tenorio-Tagle (2001) that the presence of galactic winds removes metals more efficiently from the shallower potential wells of low-mass galaxies. Sánchez Almeida et al. (2014, 2015) have argued that low metallicities in XMD galaxies are an indicator of infall of pristine gas, a process that would increase the effective yield in low-mass galaxies. Similarly, Ekta & Chengalur (2010) propose that the mechanism responsible for the metal deficiency of XMD galaxies is a better mixing in the ISM, where low-metallicity gas from large galactocentric radii dilutes the central, metal-rich gas (see also Lee, Salzer & Melbourne 2004; Kewley, Geller & Barton 2006; Peeples, Pogge & Stanek 2009). Furthermore, recently Belfiore et al. (2019) found that the inferred outflow loading factor decreases with stellar mass. It is likely that a combination of all of them to a different degree will explain the observed increase of the effective yield with baryonic mass we observe. We reiterate that for our sample, we recover a clean correlation between $M_{\rm bar}$ and $y_{\rm eff}$ only when young galaxies are selected, as shown in Fig. 12(a).

On the other hand, older galaxies show longer depletion times, and a clear anticorrelation between $M_{\rm bar}$ and $y_{\rm eff}$. The EAGLE simulations indicate that BH feedback is important for massive galaxies ($M_{\rm bar} > 10^{10}$ $M_{\odot}$), and a crucial effect to take into account to produce the mentioned anticorrelation. Without BH feedback in the history of these massive galaxies, today their effective yield would be way higher than the one observed, as shown in Fig. 12 (d) and (e). AGN feedback would have quenched the star formation and metallicity in old, massive galaxies, which is consistent with the observed low $y_{\rm eff}$, SFE, SSFR, and gas fractions. Again, the stellar age, and not just $M_{\rm bar}$, is crucial, since young galaxies with $M_{\rm bar} > 10^{10}$ still show a correlation between $M_{\rm bar}$ and $y_{\rm eff}$. Another mechanism at play is the AGN gas heating; as mentioned in Section 4.3, by increasing $\Delta T_{\rm AGN}$ to 10^9 K, a stronger decrement in the $y_{\rm eff}$ is produced. On top of the AGN feedback effect, the depletion times for older galaxies tend to be longer compared to low-mass galaxies.

The effect of an active AGN in the history of current SF galaxies has been recently studied by Matthee & Schaye (2019) using the EAGLE simulations, finding that at masses $M_{\rm star} > 10^{10}$ $M_{\rm sun}$, the residuals in the *M*–SFR relation are anticorrelated with the relative efficiency of past BH growth, which is a proxy of the accumulated AGN feedback energy.

Additionally, another possible effect to bear in mind was explored by Vincenzo et al. (2016), who find that high values of the effective yield may be indicative of an IMF favouring massive stars (Kroupa 2001; Chabrier 2003), and/or a high mass cut-off of the IMF itself.

It is important to keep in mind the various systematic effects that could bias our results. For example, the 3 arcsec diameter optical fibre used to take the SDSS spectra could bias our estimated metallicity by providing only information of the central part for large angular size galaxies. However, the EAGLE simulations show a very good agreement with our observed metallicity, for which this effect is probably not introducing a strong systematic bias. In this sense, De Rossi et al. (2017, see their appendix A) show that aperture effects do not affect the main trends found for metallicity scaling relations in the EAGLE simulations. However, changes in the aperture can generate moderate variations of the slope and normalization of those relations; for a more detailed discussion, refer to Appendix B.

Additionally, Iglesias-Páramo et al. (2016) analysed aperture corrections to a sample of SDSS galaxies. They find that for the

Downloaded from https://academic.oup.com/mnras/article/490/1/868/5569668 by INAF Trieste (Osservatorio Astronomico di Trieste) user on 05 November 2020

redshift range $0.02 < z < 0.05$, the average difference between fibre-based and integrated gas metallicities (estimated through the O3N2 index) would be of 0.034, 0.035, 0.037, 0.013, and 0.013 for the following stellar mass ranges in $\log(M_{\rm star}/{\rm M}_\odot)$: 8.5–9.1, 9.1–9.7, 9.7–10.3, 10.3–10.9, and 10.9–11.5, respectively. Even though the metallicity method is different than the one we are using in this paper, the largest metallicity over estimation would occur when $\log(M_{\rm star}/{\rm M}_\odot) < 10.3$.

Another important bias could arise from the different spatial resolution between our optical and radio data, since the ALFA has a beam size of 3.5 arcmin, quite larger in comparison with the 3 arcsec fibre used by SDSS. However, our data again show a good agreement with the EAGLE simulations when using different apertures to measure SF gas associated with H II regions ($R_{\rm ap} = 30$ kpc) and hydrogen mass ($R_{\rm ap} = 70$ kpc, Section 4.1). Furthermore, we have performed additional tests adopting the same aperture (30 and 70 kpc) when estimating the latter simulated quantities, obtaining similar general trends to those reported here for the $M_{\rm bar}$–$y_{\rm eff}$ relation, with only moderate changes in the slope and zero-point (see Appendix B). In this context, it is also worth emphasizing that De Rossi et al. (2017, see their fig. 7) were able to reproduce the observed anticorrelation between $y_{\rm eff}$ and $M_{\rm bar}$ at high masses by measuring these properties within 30 kpc and considering only the total gas mass associated with the star-forming component of the ISM. Finally, in Appendix B, we performed several tests, recalculating properties for EAGLE galaxies using different apertures. Such results suggest that the very general trends reported here are robust against aperture effects: (1) There is a correlation between $M_{\rm bar}$ and $y_{\rm eff}$ at low masses. (2) There is an anticorrelation between $M_{\rm bar}$ and $y_{\rm eff}$ at high masses. (3) At a fixed mass, $y_{\rm eff}$ shows secondary dependences on gas fraction, SFE, SSFR, and age.

In order to quantify the extent of the circumgalactic medium (CGM) and the fibre effect of the SDSS spectra, we consider an approach to measure the fraction of the protocloud originally involved in the chemical evolution of the galaxy. By considering an inside-out scenario for galaxy formation (e.g. Perez et al. 2013), we can do a rough estimate of the original protocloud assuming a closed-box model. First, we use equation (1) to estimate the gas fraction of the protocloud involved in the chemical evolution assuming a $y_{\rm true} \sim 0.002\,68$ (Pilyugin et al. 2004), and the current gas metallicity provided by SDSS. Next, we use equation (12) to solve for the gas mass of the protocloud ($M_{\rm gas_p}$). We define the baryonic mass fraction of the protocloud involved in the chemical evolution as

$$\mu_{\rm p} = (M_{\rm gas} + M_{\rm star}) \,/\, (M_{\rm gas_p} + M_{\rm star})\,. \tag{23}$$

In Fig. 13, we show $\mu_{\rm p}$ as a function of the stellar mass and gas metallicity. It is well known that galaxies show a gradient in gas metallicity from the centre to the outskirts of galaxies. The typical value of the radial abundance gradient is ∼0.2 dex/R25 (e.g. Pilyugin et al. 2019). Therefore, the 3 arcsec fibre used to obtain the SDSS spectra introduces a bias towards the centre of the SDSS galaxies, thus, providing systematically higher metallicities for some galaxies. In order to establish upper and lower limits for this systematic effect, we estimate the mass fraction of the protocloud as indicated in equation (23) for two cases: (i) the observed metallicity (Fig. 13, green contours), and (ii) for $12 + \log({\rm O/H}) - 0.2$ (Fig. 13, black contours). In the same figure, the red diamonds and blue circles correspond to galaxies from the EAGLE simulation Recal and the Virgo cluster, respectively. Note that in comparison with Iglesias-Páramo et al. (2016), we are using a larger difference of ∼0.2 dex.

It is clear from Fig. 13 that for most galaxies the fraction of the protocloud is lower than the total baryonic mass. Furthermore, there is a linear trend, where $\mu_{\rm p}$ increases with stellar mass. This approximation supports the idea that low-mass galaxies have a gas-rich CGM. On the other hand, galaxies on the right-hand side of the dashed line in Fig. 13 show galaxies with a deficit of baryonic material. The most likely scenario is that galaxies located here have suffered from removal of gas due to processes such as ram-pressure stripping. Therefore, environmental effects must play a major role here. In fact, ∼82 per cent of galaxies from the Virgo cluster are systematically located here.

7 SUMMARY AND CONCLUSIONS

In this paper, we have combined optical and radio data from the SDSS and ALFALFA surveys to create a statistically significant sample. Moreover, we have used additional data from the radio surveys GASS, COLD GASS, and a sample from the Virgo survey with optical and radio information. Throughout this paper, we focused only on star-forming galaxies selected with the BPT diagram. Also, we applied a completeness limit criterion to build a robust and reliable sample of galaxies. We analysed scaling relations between several optical (e.g. SFR, gas metallicity) and combined optical/radio (e.g. $y_{\rm eff}$, SFE, $t_{\rm dep}$, $M_{\rm bar}$) properties of galaxies. Additionally, we have compared our results with those of the EAGLE simulations. A summary of our findings is listed here:

(i) We find that ∼98 per cent of our SF sample has higher $y_{\rm eff}$ than the closed-box model prediction of $\log(y_0) = -2.57$ (Pilyugin et al. 2004).

(ii) Scaling relations with gas fraction show a smooth increment with SSFR, and an anticorrelation with SFE. This suggests that galaxies with high gas fractions are producing a high amount of stars per unit of stellar mass, although are less efficient at transforming mass into stars in comparison with galaxies with low gas fractions.

(iii) The SFE relationships with $M_{\rm star}$ and $M_{\rm bar}$–SFE are very different. While the SFE increases linearly with $M_{\rm star}$, the SFE suggests a bimodality with $M_{\rm bar}$ (within the high dispersion), where galaxies with low $M_{\rm bar}$ show a higher SFE that decreases as $M_{\rm bar}$ increases, while galaxies with a high $M_{\rm bar}$ show a high dispersion.

(iv) We use the colour excess $E(B-V)_{\rm gas}$ as indicative of extinction, finding a smooth increasing relation when $\log(M_{\rm bar}) > 9.5$. For lower values of $M_{\rm bar}$, this relation seems to flatten at $E(B-V)_{\rm gas} \sim 0.15$, suggesting lower amounts of dust for these galaxies.

(v) We find a bimodal distribution between effective oxygen yields and $M_{\rm bar}$, suggesting a relation between them when $\log(M_{\rm bar}) \lesssim 10$, in good agreement with the XMD galaxies from Ekta & Chengalur (2010). For higher values of $M_{\rm bar}$, our data suggest an anticorrelation.

(vi) To gain a deeper understanding of our observational results, we use a set of four different EAGLE simulations: Recal-L025N0752, Ref-L050N0752, AGNdT9-L050N0752, and NO-AGN-L050N0752. We compare directly the results of the Recal-L025N0752 simulation with our scaling relations, finding an excellent agreement. Indeed, we were able to even reproduce the bimodality observed in the $M_{\rm bar}$–$y_{\rm eff}$ relation.

(vii) To obtain a better interpretation of the SFE behaviour for galaxies of different masses, we analysed the $M_{\rm bar}$–$y_{\rm eff}$ relations in bins of SFE. We find that the SFE does not offer a clear bimodality of this relation. Indeed, for low SFE, galaxies are predominantly old, and there is an anticorrelation between $M_{\rm bar}$ and $y_{\rm eff}$. However,

Downloaded from https://academic.oup.com/mnras/article/490/1/868/5569668 by INAF Trieste (Osservatorio Astronomico di Trieste) user on 05 November 2020

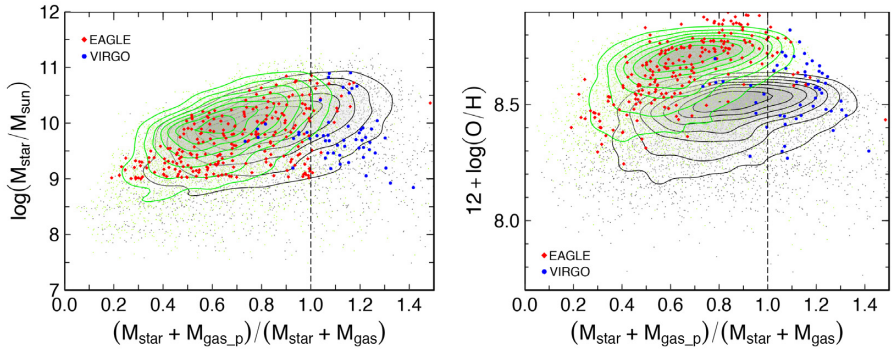

Figure 13. Mass fraction of the protocloud estimated as in equation (23) versus stellar mass (left), and gas metallicity (right). The green contours show the protocloud estimations using the measured metallicity, while the black contours show the upper limit 12 + log(O/H) minus 0.2 dex, assuming a typical gradient of ∼0.2 dex/R25 (e.g. Pilyugin et al. 2019). The red diamonds and blue circles show data from the Recal EAGLE simulations and the Virgo cluster, respectively.

galaxies with a high SFE [log(SFE) > −9.8] show a clear bimodality for the same relation, where there is an indication of a correlation for log($M_{\rm bar}$) < 10, and an anticorrelation for higher masses. A comparison with the EAGLE simulation Recal shows a very good agreement. The model NO-AGN, in which AGN feedback is suppressed, is not able to reproduce the drop in $y_{\rm eff}$ observed for the higher SFE bins. Therefore, the inclusion of AGN feedback is very important to reproduce the observations.

(viii) We analysed in more detail the $M_{\rm bar}$–$y_{\rm eff}$ relationship for a subsample of galaxies with direct measurements of stellar age. We find that this relationship, with an apparent high dispersion, can be separated in clean correlations and anticorrelations when bins of stellar age are taken. For young galaxies, the $y_{\rm eff}$ increases with $M_{\rm bar}$; furthermore, XMD galaxies from Ekta & Chengalur (2010) are in good agreement with this subsample. As the bins in stellar age increase, the $M_{\rm bar}$–$y_{\rm eff}$ relation starts to flatten until it becomes an anticorrelation for log($t_{\rm r}$) > 9.4 yr. The 'Recal' simulation predicts the correlations and anticorrelation observed in this relation. Furthermore, the simulations predict that young, low-mass systems are not significantly affected by AGN feedback. However, as age and baryonic mass increase, AGN feedback effects seem to be stronger, leading to an anticorrelation. Furthermore, the 'NO-AGN' model predicts a correlation between the same variables.

(ix) By using a rough estimation of the original protocloud of the galaxy, we find that low-mass galaxies have a gas-rich CGM. Furthermore, the CGM decreases as galaxies convert gas into stars, thus increasing their stellar mass. We find that the baryonic mass of the protocloud can be used to identify galaxies that have experienced intense loss of baryonic material.

(x) Among the possible reasons of why the effective yield changes, it is likely that several mechanisms are playing a role, and that their degree of impact depends strongly on the age and baryonic mass of the galaxies.

(a) For young galaxies with predominantly low $M_{\rm bar}$, it has been argued that the presence of galactic winds would remove metals more efficiently from the shallower potential wells of low-mass galaxies, which would result in a higher $y_{\rm eff}$. Furthermore, the infall of pristine gas would increase the effective yield as well. A combination of both the processes is likely to produce a correlation between $y_{\rm eff}$ and $M_{\rm bar}$. Additionally, this tendency is stronger for young galaxies, which also show faster depletion times.

(b) For old galaxies, predominantly with log($M_{\rm bar}$) $\gtrsim$ 10 $M_\odot$, the most important mechanism at play is likely to be a past AGN feedback effect, which would have quenched the SFR and chemical evolution of the galaxy. In this case, only gas-rich mergers or significant gas accretion events might lead to further evolution. The EAGLE simulation Recal is able to reproduce the observed anticorrelation between $y_{\rm eff}$ and $M_{\rm bar}$; also, the NO-AGN model is not able to reproduce this anticorrelation. Furthermore, the EAGLE simulation AGNdT9, which implements a higher temperature increment associated with AGN heating ($\Delta T_{\rm AGN} = 10^9$ K), leads to a stronger decrease of $y_{\rm eff}$ at higher $M_{\rm bar}$. Therefore, different AGN heating temperatures could be affecting and decreasing the $y_{\rm eff}$ in different degrees.

(xi) Placing our results in the downsizing scenario, young galaxies show predominantly low masses (although can extend up to $M_{\rm bar} \sim 10^{10.5}$ $M_\odot$), show faster depletion times, and do not seem to have been affected by an active AGN in their history. On the other hand, older galaxies are predominantly massive ($M_{\rm bar} > 10^{10}$ $M_\odot$), show on average longer depletion times, and AGN feedback must have played an important role in their history by quenching their SFR.

ACKNOWLEDGEMENTS

We thank Shane O'Sullivan for insightful discussion. We also thank the anonymous referees for their careful reading of this manuscript and helpful comments. MEDR acknowledges support from PICT-2015-3125 of ANPCyT, PIP 112-201501-00447 of CONICET, and UNLP G151 of UNLP (Argentina). AG acknowledges support by the INAF PRIN-SKA2017 programme 1.05.01.88.04.ESKAPE-HI. TMH acknowledges the support from the Chinese Academy of Sciences (CAS) and the National Commission for Scientific and Technological Research of Chile (CONICYT) through a CAS-CONICYT Joint Postdoctoral Fellowship administered by the CAS South America Center for Astronomy (CASSACA) in Santiago, Chile. IAZ acknowledges the support of the National Academy of Sciences of Ukraine by the grant 417Kt. Funding for the SDSS and SDSS-II has been provided by the Alfred P. Sloan Foundation, the Participating Institutions, the National Science Foundation, the U.S. Department of Energy, the National Aeronautics and Space Administration, the Japanese Monbukagakusho, the Max Planck Society, and the Higher Education Funding Council for England. The SDSS web site is http://www.sdss.org/. We acknowledge the Virgo Consortium for making their simulation data available. The EAGLE simulations were performed using the DiRAC-2 facility at Durham, managed by the ICC, and the PRACE facility Curie based

Downloaded from https://academic.oup.com/mnras/article/490/1/868/5569668 by INAF Trieste (Osservatorio Astronomico di Trieste) user on 05 November 2020

in France at TGCC, CEA, Bruyères-le-Châtel. This work used the DiRAC@Durham facility managed by the Institute for Computational Cosmology on behalf of the STFC DiRAC HPC Facility (www.dirac.ac.uk). The equipment was funded by BEIS capital funding via STFC capital grants ST/P002293/1, ST/R002371/1, and ST/S002502/1, Durham University, and STFC operations grant ST/R000832/1. DiRAC is part of the National e-Infrastructure. We have benefited from the publicly available 'R' statistical programing language (http://www.R-project.org/) and the TOPCAT analysis tool (http://www.starlink.ac.uk/topcat/).

REFERENCES

Abazajian K. N. et al., 2009, ApJS, 182, 543
Albareti F. D. et al., 2017, ApJS, 233, 25
Baldwin J., Phillips M., Terlevich R., 1981, PASP, 93, 5(BPT)
Belfiore F., Vincenzo F., Maiolino R., Matteucci F., 2019, MNRAS, 487, 456
Bothwell M. S., Maiolino R., Kennicutt R., Cresci G., Mannucci F., Marconi A., Cicone C., 2013, MNRAS, 433, 1425
Brinchmann J., Charlot S., White S. D. M., Tremonti C., Kauffmann G., Heckman T., Brinkmann J., 2004, MNRAS, 351, 1151
Brooks A. M., Governato F., Quinn T., Brook C. B., Wadsley J., 2009, ApJ, 694, 396
Brough S. et al., 2011, MNRAS, 413, 1236
Bruzual G., Charlot S., 2003, MNRAS, 344, 1000
Calura F., Pipino A., Chiappini C., Matteucci F., Maiolino R., 2009, A&A, 504, 373
Calzetti D., Kinney A. L., Storchi-Bergmann T., 1994, ApJ, 429, 582
Calzetti D., Kinney A. L., Storchi-Bergmann T., 1996, ApJ, 458, 132
Calzetti D., Armus L., Bohlin R. C., Kinney A. L., Koornneef J., Storchi-Bergmann T., 2000, ApJ, 533, 682
Catinella B. et al., 2010, MNRAS, 403, 683
Chabrier G., 2003, PASP, 115, 763
Crain R. A. et al., 2015, MNRAS, 450, 1937
Crain R. A. et al., 2017, MNRAS, 464, 4204
Dalcanton J. J., 2007, ApJ, 658, 941
De Rossi M. E., Bower R. G., Font A. S., Schaye J., Theuns T., 2017, MNRAS, 472, 3354
De Rossi M. E., Bower R. G., Font A. S., Schaye T., 2018, BAAA, 60, 121
Duarte Puertas S., Vilchez J. M., Iglesias-Páramo J., Kehrig C., Pérez-Montero E., Rosales-Ortega F. F., 2017, A&A, 599, A71
Edmunds M. G., 1990, MNRAS, 246, 678
Ekta B., Chengalur J. N., 2010, MNRAS, 406, 1238
Ellison S. L., Sánchez S. F., Ibarra-Medel H., Antonio B., Mendel J. T., Barrera-Ballesteros J., 2018, MNRAS, 474, 2039
Espíritu J. N., Peimbert A., Delgado-Inglada G., Ruiz M. T., 2017, Rev. Mex. Astron. Astrofis., 53, 95
Filho M. E. et al., 2013, A&A, 558, A18
Finlator K., Davé R., 2008, MNRAS, 385, 2181
Fontanot F., De Lucia G., Monaco P., Somerville R. S., Santini P., 2009, MNRAS, 397, 1776
Gallazzi A., Charlot S., Brinchmann J., White S. D. M., Tremonti C. A., 2005, MNRAS, 362, 41
Garnett D. R., 2002, ApJ, 581, 1019
Giovanelli R. et al., 2005, AJ, 130, 2598
Gunawardhana M. L. P. et al., 2011, MNRAS, 415, 1647
Gunn J. E. et al., 2006, AJ, 131, 2332
Haynes M. P. et al., 2011, AJ, 142, 170
Hopkins A. M. et al., 2003, ApJ, 599, 971
Hughes T. M., Cortese L., Boselli A., Gavazzi G., Davies J. I., 2013, A&A, 550, A115
Iglesias-Páramo J. et al., 2016, ApJ, 826, 71
Kauffmann G. et al., 2003a, MNRAS, 341, 33
Kauffmann G. et al., 2003b, MNRAS, 346, 1055
Kauffmann G. et al., 2003c, MNRAS, 341, 54
Kennicutt R. C. Jr, 1998, ApJ, 498, 541
Kewley L. J., Geller M. J., Barton E. J., 2006, AJ, 131, 2004
Köppen J., Weidner C., Kroupa P., 2007, MNRAS, 375, 673
Kroupa P., 2001, MNRAS, 322, 231
Kudritzki R.-P., Ho I.-T., Schruba A., Burkert A., Zahid H. J., Bresolin F., Dima G. I., 2015, MNRAS, 450, 342
Lara-López M. A., Cepa J., Bongiovanni A., Pérez García A. M., Castañeda H., Fernández Lorenzo M., Pović M., Sánchez-Portal M., 2009, A&A, 505, 529
Lara-López M. A., Bongiovanni A., Cepa J., Pérez García A. M., Sánchez-Portal M., Castañeda H. O., Fernández Lorenzo M., Pović M., 2010, A&A, 519, A31
Lara-López M. A. et al., 2013a, MNRAS, 434, 451
Lara-López M. A. et al., 2013b, MNRAS, 434, L35
Larson R. B., 1974, MNRAS, 169, 229
Lee J. C., Salzer J. J., Melbourne J., 2004, ApJ, 616, 752
Lee H., Skillman E. D., Cannon J. M., Jackson D. C., Gehrz R. D., Polomski E. F., Woodward C. E., 2006, ApJ, 647, 970
Leroy A. K., Walter F., Brinks E., Bigiel F., de Blok W. J. G., Madore B., Thornley M. D., 2008, AJ, 136, 2782
McAlpine S. et al., 2016, Astron. Comput., 15, 72
Marasco A., Crain R. A., Schaye J., Bahé Y. M., van der Hulst T., Theuns T., Bower R. G., 2016, MNRAS, 461, 2630
Matthee J., Schaye J., 2019, MNRAS, 484, 915
Mesa-Delgado A., Esteban C., García-Rojas J., Luridiana V., Bautista M., Rodríguez M., López-Martín L., Peimbert M., 2009, MNRAS, 395, 855
Mollá M., Cavichia O., Gavilán M., Gibson B. K., 2015, MNRAS, 451, 3693
Neistein E., van den Bosch F. C., Dekel A., 2006, MNRAS, 372, 933
Noeske K. G. et al., 2007, ApJ, 660, L43
Osterbrock D. E., 1989, Astrophysics of Gaseous Nebulae and Active Galactic Nuclei. Univ. Sci. Books, Mill Valley, CA
Pagel B. E. J., Patchett B. E., 1975, MNRAS, 172, 13
Peeples M. S., Pogge R. W., Stanek K. Z., 2009, ApJ, 695, 259
Peimbert A., Peimbert M., 2010, ApJ, 724, 791
Perez E. et al., 2013, ApJ, 764, L1
Pettini M., Pagel B. E. J., 2004, MNRAS, 348, L59
Pilyugin L. S., Grebel E. K., 2016, MNRAS, 457, 3678
Pilyugin L. S., Vílchez J. M., Contini T., 2004, A&A, 425, 849
Pilyugin L. S., Thuan T. X., Vílchez J. M., 2007, MNRAS, 376, 353
Pilyugin L. S., Grebel E. K., Zinchenko I. A., Nefedyev Y. A., Shulga V. M., Han V., Berczik P. P., 2018, A&A, 613, A1
Pilyugin L. S., Grebel E. K., Zinchenko I. A., Nefedyev Y. A., Vílchez J. M., 2019, A&A, 623, A122
Pozzetti L. et al., 2010, A&A, 523, A13
Robotham A. S. G., Obreschkow D., 2015, Publ. Astron. Soc. Aust., 32, e033
Saintonge A. et al., 2011, MNRAS, 415, 32
Sánchez Almeida J., Morales-Luis A. B., Muñoz-Tuñón C., Elmegreen D. M., Elmegreen B. G., Méndez-Abreu J., 2014, ApJ, 783, 45
Sánchez Almeida J. et al., 2015, ApJ, 810, L15
Schaye J. et al., 2015, MNRAS, 446, 521
Searle L., Sargent W. L. W., 1972, ApJ, 173, 25
Silich S., Tenorio-Tagle G., 2001, ApJ, 552, 91
Springel V., 2005, MNRAS, 364, 1105
Strauss M. A. et al., 2002, AJ, 124, 1810
Talbot R. J. Jr, Arnett W. D., 1971, ApJ, 170, 409
Telford O. G., Werk J. K., Dalcanton J. J., Williams B. F., 2019, ApJ, 877, 120
The EAGLE Team, 2017, preprint (arXiv:1706.09899)
Thomas D., Maraston C., Bender R., Mendes de Oliveira C., 2005, ApJ, 621, 673
Thuan T. X., Lecavelier des Etangs A., Izotov Y. I., 2005, ApJ, 621, 269
Thuan T. X., Goehring K. M., Hibbard J. E., Izotov Y. I., Hunt L. K., 2016, MNRAS, 463, 4268
Tremonti C. A. et al., 2004, ApJ, 613, 898
Vale Asari N., Stasińska G., Cid Fernandes R., Gomes J. M., Schlickmann M., Mateus A., Schoenell W., 2009, MNRAS, 396, L71

Downloaded from https://academic.oup.com/mnras/article/490/1/868/5569668 by INAF Trieste (Osservatorio Astronomico di Trieste) user on 05 November 2020

Vílchez J. M., Relaño M., Kennicutt R., De Looze I., Mollá M., Galametz M., 2019, MNRAS, 483, 4968
Vincenzo F., Matteucci F., Belfiore F., Maiolino R., 2016, MNRAS, 455, 4183
Zasov A., Saburova A., Abramova O., 2015, AJ, 150, 192

APPENDIX A: COMPARISON OF SFRS AND GAS METALLICITIES WITH OTHER DATABASES

With the aim of identify possible biases affecting our SFRs, in this section we perform a comparison between the SFRs used in this paper by Brinchmann et al. (2004), the SFR estimated by Duarte Puertas et al. (2017) using correction prescribed from IFU data, and direct integrated IFU MaNGA-DR14 SFRs estimated by us. We find 59 MANGA-SDSS/ALFALFA counterparts, and 25 common counterparts in the 3 catalogues.

In Fig. A1 left, we present a histogram of the log(SFR) difference between MaNGA and Brinchmann et al. (2004) in blue, and MaNGA and Duarte Puertas et al. (2017) in red for the 25 galaxies in common in the 3 catalogues. The mean difference between the integrated log(SFR) of MaNGA and Brinchmann et al. (2004) is ∼0.026 dex, while for MaNGA and Duarte Puertas et al. (2017) is ∼0.03 dex. Furthermore, using the whole SDSS-DR 7 sample, Ellison et al. (2018) found 394 counterparts with MaNGA DR13 (Albareti et al. 2017), finding that the mean log(SFR) difference between Brinchmann et al. (2004) and integrated MaNGA values is ∼0.03 dex.

In Fig. A1 right, we show a histogram with the gas metallicity difference between the 59 MaNGA and SDSS/ALFALFA counterparts. Metallicities were estimated consistently for the two data sets as indicated in Section 2.1 of this paper, using integrated the IFU MaNGA data, and single 3 arcsec fibre for the SDSS/ALFALFA data. We find that the mean difference in $12 + \log(O/H)$ is ∼0.03 dex.

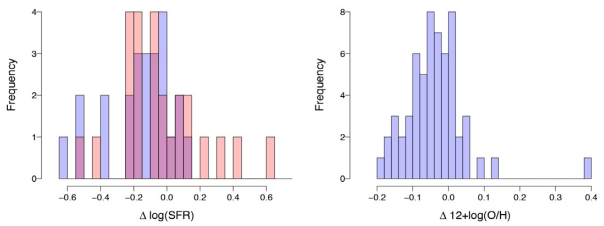

Figure A1. Comparison between different SFRs and metallicities. Left: The histograms show the difference between MaNGA and Brinchmann et al. (2004) SFRs (blue), and MaNGA and Duarte Puertas et al. (2017) (red), for 25 common sources between the 3 catalogues. Right: The blue histogram shows the difference between integrated IFU MaNGA and 3 arcsec fibre SDSS/ALFALFA gas metallicities estimated in this work for 59 common sources.

APPENDIX B: SIMULATED DATA USING DIFFERENT APERTURES

In this section, we present results from the EAGLE simulations considering different apertures when estimating galaxy properties.

In Fig. B1, all properties were calculated similarly to those shown in the top panel of Fig. 10, with the only exception of metallicities, which were evaluated at different apertures R_Z, as shown in the different panels. We consider a minimum R_Z of ≈1.75 kpc, which is close to the smallest apertures associated with metallicity estimates for the SDSS sample. We see that a decrease of R_Z generates a slight variation in the shape of the M_{bar}–y_{eff} relation and a moderate increase of effective yields ($\lesssim$0.5 dex), with the most significant variations in the case of gas-rich galaxies. However, it is clear that the main trends of the M_{bar}–y_{eff} relation are preserved when varying R_Z: there is a correlation at the low-mass end and an anticorrelation at the high-mass end. Also, at a fixed mass, the secondary dependences of y_{eff} on gas fraction, SFE, SSFR, and t_r are still present at small R_Z.

In Fig. B2, we show results from the EAGLE simulations when evaluating all galaxy properties at the same fix aperture of 30 kpc (top panel) and 70 kpc (bottom panel). When comparing with Fig. 10 (top panels), we see that the main trends of the relationships are preserved, although variations in the slope and normalization are present. The most significant variations are obtained when measuring all properties at $\lesssim$30 kpc because of the decrease of the total gas mass with respect to our *default* value for this quantity, which was measured at $\lesssim$70 kpc. On the other hand, not very significant changes with respect to Fig. 10 are obtained when evaluating all quantities at $\lesssim$70 kpc. This is a consequence of the fact that the simulated stellar component and star-forming gas phase (used to estimate metallicities) tend to be located in the central regions of galaxies ($\lesssim$30 kpc).

We conclude that our main findings are robust against aperture effects.

Downloaded from https://academic.oup.com/mnras/article/490/1/868/5569668 by INAF Trieste (Osservatorio Astronomico di Trieste) user on 05 November 2020

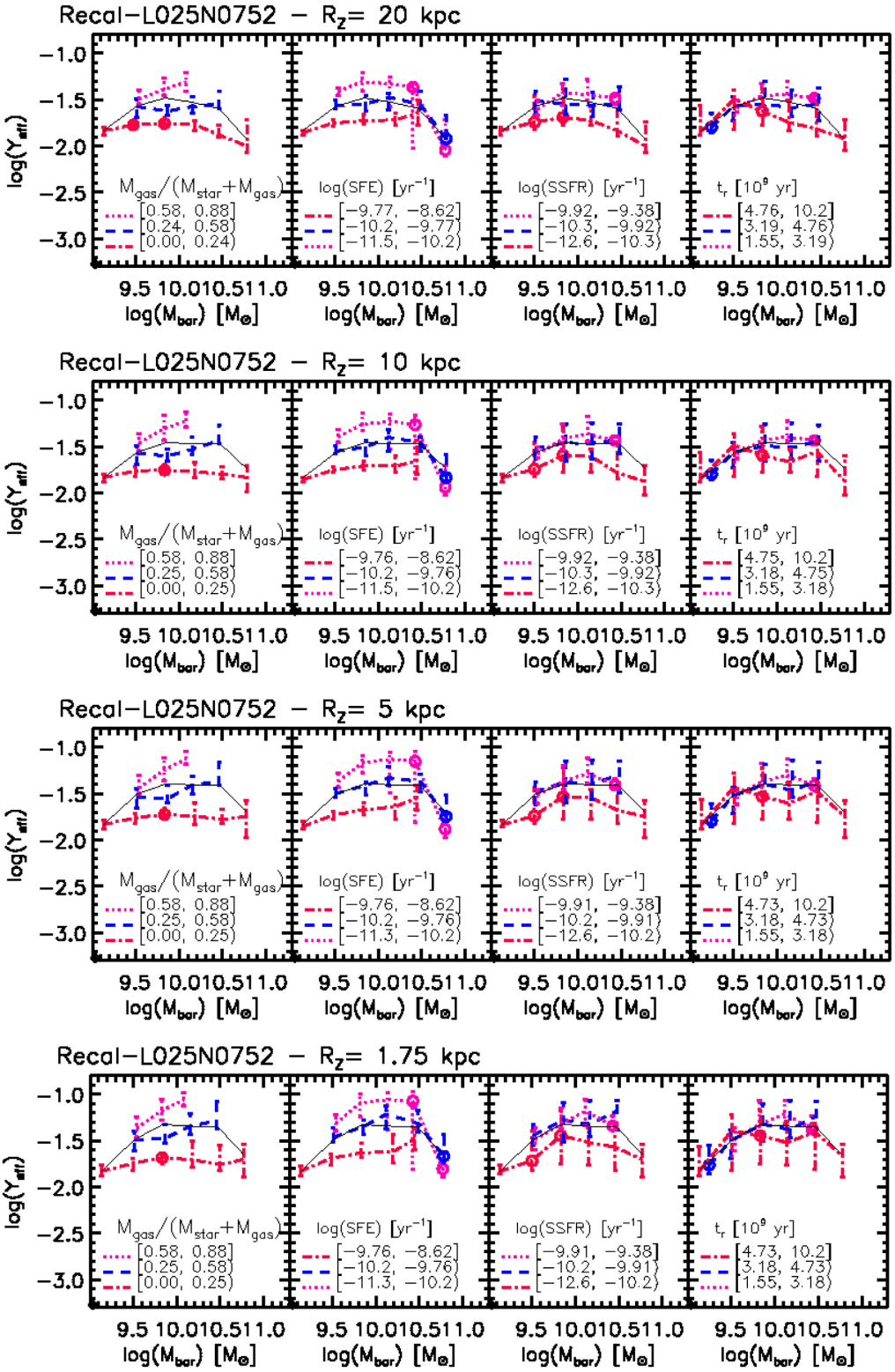

Figure B1. Effective yields as a function of baryonic mass for the EAGLE simulation Recal-L025N0752. Metallicities here have been estimated using different fix apertures R_Z (see the title of each panel), while all other properties were calculated using similar apertures to those used in Fig. 10 (top panel). Note that, for Fig. 10, $R_Z = 30$ kpc.

Downloaded from https://academic.oup.com/mnras/article/490/1/868/5569668 by INAF Trieste (Osservatorio Astronomico di Trieste) user on 05 November 2020

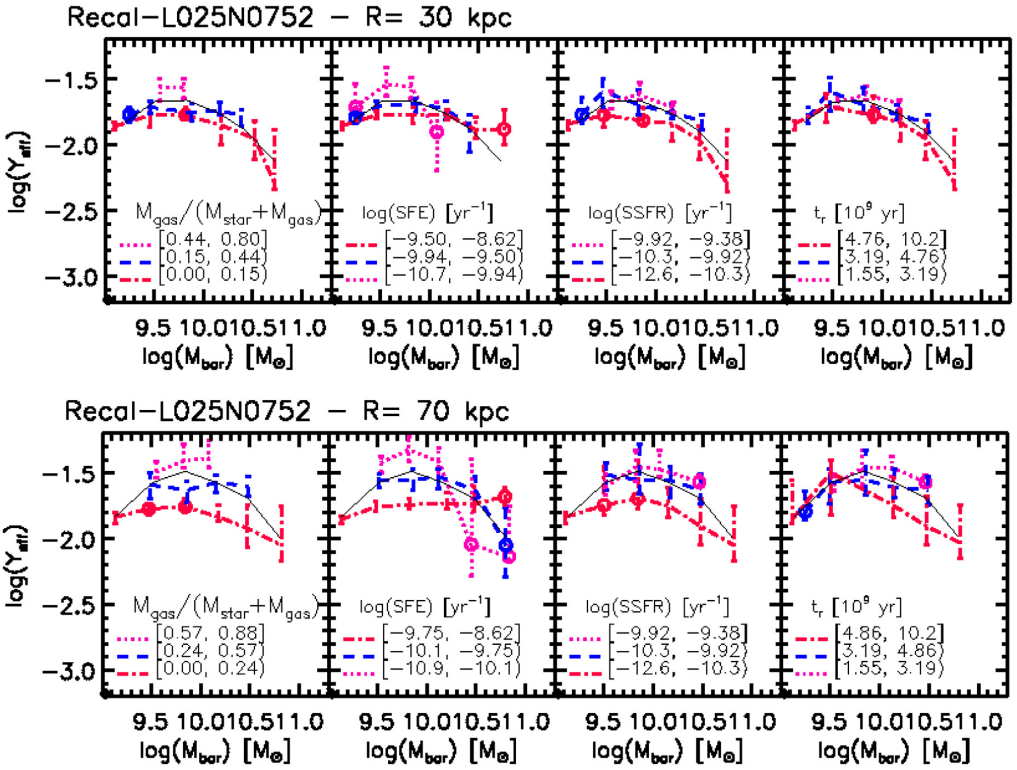

Figure B2. Effective yields as a function of baryonic mass for the EAGLE simulation Recal-L025N0752. In contrast with Fig. 10 (top panel), in the top panel here, all properties have been estimated using a fix aperture of 30 kpc. In the bottom panel, all properties were estimated using a fix aperture of 70 kpc, with the only exception of the age (t_r). The luminosity-weighted age t_r was estimated using an aperture of 30 kpc as the EAGLE data base does not provide luminosities at larger apertures.

This paper has been typeset from a TEX/LATEX file prepared by the author.

Downloaded from https://academic.oup.com/mnras/article/490/1/868/5569668 by INAF Trieste (Osservatorio Astronomico di Trieste) user on 05 November 2020